Pergamon

J. Biomechanics, Vol. 27, No. 3, pp. 339–360, 1994

0021-9290/94 $6.00 + .00

A MODEL FOR THE EXCITATION OF OSTEOCYTES BY MECHANICAL LOADING-INDUCED BONE FLUID SHEAR STRESSES

S. WEINBAUM, S. C. COWIN and YU ZENG

Department of Mechanical Engineering, The School of Engineering of The City College and The Graduate School of The City University of New York, New York, NY 10031, U.S.A.

Abstract—A new experimentally testable hypothesis is advanced for the mechanosensory transduction mechanism by which communicating osteocytes sense the very small *in vivo* strains in the calcified matrix components of bone. We propose that the osteocytes, although not responsive to substantial fluid pressures, can be stimulated by relatively small fluid shear stresses acting on the membranes of their osteocytic processes. Biot's porous media theory is used to relate the combined axial and bending loads applied to a whole bone to the flow past the osteocytic processes in their canaliculi. In this theory, the bone pores of interest are the proteoglycan filled fluid annuli that surround the osteocytic processes in the canaliculi. We show that previously predicted fluid pore pressure relaxation times were a hundred-fold too short for the lacunar–canalicular porosity because they neglected the fluid drag associated with proteoglycan matrix on the surface membrane of the osteocyte and its cell processes. The recent theory developed in Tsay and Weinbaum [*J. Fluid Mech.* **226,** 125–148 (1991)] for flow through cross-linked fiber filled channels is used to model the flow through this proteoglycan matrix. The predicted pore relaxation time, 1–2 s, closely corresponds to the times measured by Salzstein and Pollack [*J. Biomechanics* **20,** 271–280 (1987)]. Furthermore, using this model, the magnitude of the predicted fluid induced shear stresses, 8–30 dyn cm^{-2}, is shown to be similar to the fluid shear stresses measured in osteoblasts and other cells in which an intracellular Ca^{2+} shear stress response had been observed. This model is also used, in conjunction with anatomical data and the pore fluid pressure relaxation time data, to show that the spacing between the fibers is approximately 7 nm. The result is consistent with the notion that the canalicular pore space is filled with glycosaminoglycans that are ordered by albumin according to the model of Michel [*J. Physiol.* **404,** 1–29 (1988)]. The new hypothesis is also shown to be consistent with the experiments of McLeod *et al.* [*J. Biomechanics* (submitted)] which suggest that high-frequency low-amplitude postural strains can maintain and even increase bone mass.

NOMENCLATURE AND VALUES OF PARAMETERS EMPLOYED

a	radius of the osteocytic process
a_0	radius of a fiber
b	radius of the canaliculus
B	dimensionless relative compressibility constant which is a ratio of the increment in pore water pressure to the increment in the sum of the three normal stresses in the solid matrix under undrained conditions ($B \approx 0.53$)
c	diffusion coefficient in the differential equation governing the pore fluid pressure ($=H_A k$ in Salzstein *et al.* (1987)
d	the half thickness of a trabecula, or the radius of an osteon, or the half thickness of the bone specimen in the four-point bending apparatus experiments
G	shear modulus of the solid bone matrix under 'drained' conditions ($G \approx 6$ GPa)
GAG	glycosaminoglycans
i	$\sqrt{-1}$
I	area moment of inertia per unit length of the cross-sectional area of the tissue or slab specimen
I_0, I_1, I_2	modified Bessel functions of the first kind (same in Salzstein *et al.*).
K_0, K_1, K_2	modified Bessel functions of the third kind or Macdonald's functions (same in Salzstein *et al.*)
k	the Darcy law permeability constant at the lacunar–canalicular porosity scale, related to the coefficient of permeability κ by $\kappa = k/\mu$, where μ is the fluid viscosity
k_∞	the Darcy law permeability constant at the lacunar–canalicular porosity scale in the very dilute fiber limit
k_p	the Darcy law permeability constant at the fiber matrix scale for fluid flow through a net of transverse fibers
$k_{p,\mathrm{eff}}$	the Darcy law permeability constant at the cell process channel scale (which accounts for the presence of the walls of the annulus) for fluid flow through a cell process channel filled with transverse fibers
L	center-to-center spacing between lacunae; dimension of the periodic lacunar cell employed in the model
m	the magnitude of the periodic moment applied to the tissue or slab specimen
M	dimensionless ratio of the bending to the axial stress
n	number of channels in an area L by L, L being the dimension of the periodic lacunar cell employed in the model (same in Salzstein *et al.*)
p	pore fluid pressure
P	dimensionless pressure ($P = 3p/\sigma BT$)
q	the ratio of the radius of the canaliculus, b, to the radius of the osteocytic process, a ($q = b/a$)
Q	volume flow rate of the pore fluid (same in Salzstein *et al.*)
r	radial coordinate from the axis of the osteocytic process

Received in final form 1 *May* 1993.

s	shear stress acting on the surface of the osteocytic process
s_∞	shear stress acting on the surface of the osteocytic process in the very dilute fiber limit
t	time (same in Salzstein *et al.*)
T	dimensionless frequency parameter ($T=\omega d^2 c^{-1}=\tau_r/\tau_f$)
T_{kk}	sum of the three normal Cartesian stress tensor components of the total stress
T_{zz}	the z normal component of the Cartesian total stress tensor
$\mathbf{u}$	pore fluid velocity
u	component of the pore fluid velocity
x, y, z	rectangular coordinates (same in Salzstein *et al.*)
Y	dimensionless rectangular coordinate ($Y=yd^{-1}$)
α	dimensionless length parameter [$\alpha=(b-a)/\sqrt{k_p}$], which is the ratio of two lengths, the width of the channel between the cytoplasmic process and the wall of the canaliculus, $b-a$, and the thickness of the fiber induced boundary layer near the wall, $\sqrt{k_p}$
β	dimensionless complex number depending on dimensionless frequency parameter, [$\beta=(1+i)\sqrt{(T/2)}$]
γ	dimensionless parameter ($\gamma=b/\sqrt{k_p}$), which is the ratio of two lengths, the radius of the canaliculus b and the thickness of the fiber induced boundary layer near the wall, $\sqrt{k_p}$
Δ	spacing between the transverse fibers in the channel between the cytoplasmic process and the wall of the canaliculus
η	boundary pore fluid leakage coefficient
κ	coefficient of permeability, equal to k/μ, where μ is the fluid viscosity and the permeability constant k has the units of area and is a function of the porous bone structure only
μ	fluid viscosity (in Salzstein *et al.* $=\eta$)
ν	Poisson's ratio of the solid bone matrix under 'drained' conditions ($=H_A\lambda^s$ in Salzstein *et al.*), ($\nu_u \approx 0.25$)
ν_u	Poisson's ratio of the solid bone matrix under 'undrained' conditions ($\nu_u \approx 0.3$)
σ	the magnitude of the periodic axial compressive stress
σ_0	the magnitude of the temporally constant compressive stress
τ	dimensionless time ($\tau=ctd^{-2}=t/\tau_r$)
τ_r	characteristic time of relaxation of the fluid pore pressure ($\tau_r=d^2c^{-1}$)
τ_f	characteristic time of applied forcing ($\tau_f=\omega^{-1}$)
ω	driving frequency (same in Salzstein *et al.*)

INTRODUCTION

A new hypothesis is advanced here for the cellular level mechanosensory feedback mechanism associated with Wolff's law. The hypothesis concerns the mechanism by which the osteocytes housed in the lacunae of mechanically loaded bone sense the load applied to the bone by the detection of dynamic strains. We propose that the osteocytes are stimulated by relatively small fluid shear stresses acting on the membranes of their osteocytic processes. To explore this hypothesis, we develop a hierarchical model of bone tissue structure which relates cyclic mechanical loading applied to the whole bone to the fluid shear stress at the surface of the osteocytic cell process. In this model, the sensitivity of strain detection is a function of frequency. We show that in the physiological frequency range (1–20 Hz), associated with either locomotion (1–2 Hz) or the maintenance of posture (15–20 Hz), the fluid shear stress is nearly proportional to the product of frequency and strain. Thus, if bone cells respond to strains on the order of 0.1% at frequencies of 1 or 2 Hz, they will also respond to strains on the order of 0.01% at frequencies of 20 Hz.

There are three levels of bone porosity, all containing bone fluid. These include the vascular porosity associated with the Volkmann canals and the Haversian lumens (order 10 μm), the lacunar–canalicular porosity associated with the fluid space surrounding the osteocytes (order 0.1 μm) and the collagen–hydroxyapatite porosity associated with the spaces between the crystallites of the mineral hydroxyapatite (order 20–60 nm). Our model involves only the lacunar–canalicular porosity, which we propose is the primary porosity scale associated with the relaxation of the excess pore pressure due to mechanical loading. The movement of the bone fluid in the collagen–hydroxyapatite porosity is negligible because most of the bone water in that porosity is bound by interaction with the ionic crystal [see Neuman and Neuman (1958)]. In our model, the mature bone at the walls of the lacunar–canalicular system is assumed to be impermeable.

Our model of the lacunar–canalicular porosity is divided into three levels of scale. The smallest-scale level is the spacing Δ (approximately 7 nm) between the GAG associated with a continuous network of proteoglycans that are attached to the membrane surface of the osteocytic process via central filaments of hyaluronic acid. The middle-scale level is the gap (approximately 0.1 μm) between the wall of a canaliculus and the surface of the cell process in the canaliculus. The largest-scale level is a periodic unit cell (approximately a cubic volume 35 μm on each edge) containing a single lacuna at its center. This length is characterized by the distance between lacunae. These length-scale levels and their associated permeabilities are described in greater detail in the body of the paper.

We note that the model proposed herein differs from an earlier version first presented in Weinbaum *et al.* (1991) in that we examine here the possibility that the canalicular porosity is filled with a proteoglycan matrix that is ordered by albumin in the thin fluid layer between the walls of the canaliculi and the surface of the osteocytic process. This type of matrix has been observed to exist on the surface of all vascular endothelial cells where it serves as a filter for plasma proteins [see Michel (1988)]. In the earlier model, where this matrix was not included, the pre-

dicted pore pressure relaxation times were two orders of magnitude smaller than had been observed experimentally and the predicted fluid shear stress on the osteocytic process surface was much greater than those known to excite bone cells, for the physiologically observed dimensions of the fluid annulus.

Several investigators (Johnson, 1984; Kufahl and Saha, 1990; Piekarski and Munro, 1977) have examined other aspects of the lacunar–canalicular porosity using simple circular pore models and have attempted to analyze its possible physiological importance. These studies have primarily emphasized the importance of the convective flow in the canaliculi between the lacunae as a way of enhancing the supply of nutrients between neighboring osteocytes. Previous studies on the relaxation of the excess pore pressure have been closely tied to the strain generated potentials (SGP) associated with bone fluid motion. Pollack and coworkers (Pollack *et al.*, 1984; Salzstein *et al.*, 1987; Salzstein and Pollack, 1987) have laid an important foundation for explaining the origin of (SGP). A fundamental difference between this paper and the theoretical model in Salzstein *et al.* (1987) is that we propose that it is the lacunar–canalicular porosity and not the collagen–hydroxyapatite porosity which determines the fluid pressure relaxation time and is the conduit for the streaming potential. The latter possibility is explored in our companion paper, Cowin *et al.* (1993), where the SGP data reported by Salzstein and Pollack (1987) and by Scott and Korostoff (1990) are used to validate experimentally the hypothesized spacing, $\Delta = 7$ nm, of the glycosaminoglycans (GAGs) in the proteoglycan (PG) matrix that is assumed in this paper.

MODEL DEVELOPMENT

Model geometry

Our idealized model geometries for the three hierarchical anatomical levels of the lacunar–canalicular porosity are taken from well-accepted three-dimensional reconstructions of the lacunar–canalicular porosity (Fig. 1). These idealizations are on two length scales—the larger length scale (Fig. 2) is the center-to-center distance between lacunae, and the smaller length scale (Fig. 3) is the radius of a canaliculus. In our idealized model, the lacunae with their connecting canaliculi are arranged in a periodic three-dimensional cubic array with spacing L (Fig. 2). The illustration shows an idealized model of a trabecula in cross section. The canaliculi also contain communicating osteocytic processes (shown at the scale of Fig. 3, but not that of Fig. 2), which link not only adjacent osteocytes but also interior osteocytes with osteoblasts at the bone surface. The highlighted square insert in the diagram is the periodic unit that will be used to calculate the large-scale Darcy permeability k of the trabecula. The cuboidal periodic unit shown in Fig. 2 with a single lacuna at its center contains many (50–100) canaliculi that cross its surface. Our idealized model for an individual canaliculus with its central cell process can be viewed in either transverse cross section [Fig. 3(a)] or longitudinal cross section [Fig. 3(b)]. A communicating junction connecting cell processes is also shown in the longitudinal cross section. In our idealized model, the concentric circular cylindrical fluid annulus of thickness $(b-a)$ between the surface of the osteocytic cell membrane and the surface of the canalicular wall contains a proteoglycan matrix which is schematically shown by shaded cross-bridging fibers with an open gap Δ between them. The spacing Δ is the characteristic distance between the GAG sidechains of the core proteins of the proteoglycan subunits. This spacing Δ is only shown symbolically since the actual arrangement of the GAG, core proteins and hyaluronic acid central filaments cannot (yet) be observed at this scale.

We propose that the surface glycocalyx on the osteocytic membrane is very similar to that observed on vascular endothelial cells where ruthenium red staining first suggested matrix components of PG aggregates extending 0.1 μm or more from the cell surface [see Luft (1966)]. The PG matrix is composed of three basic structural elements, GAG, core proteins and hyaluronic acid (HA). Our hypothesized arrangement of these components in the fluid annulus (Fig. 4) is based on a sketch taken from Curry (1986) in which the surface glycocalyx of endothelial cells is depicted. GAG sidechains of typically 0.6 nm radius surround the core proteins (2 nm radius) and the latter are linked at their base by the long chain hyaluronic acid molecules, which are the actual spanning fibers in the annulus. A central feature of the surface glycocalyx is that it is now generally believed to be ordered by albumin [see Michel (1988)]. Michel has shown that the positive arginine groups at the ends of the albumin attach to the negatively charged GAG. This electrostatic interaction orders the GAG and requires the spacing Δ to be of the same order as the albumin molecule, 7 nm. The hypothesized aggregated PG matrix associated with the surface glycocalyx of an osteocyte differs substantially from the small nonaggregating chondroitin sulphate PGs (i.e. decorin and PG-S1 biglycan) in the volume of the mineralized bone matrix [see Poole (1986) and Heinegård and Oldberg (1989)]. These small nonaggregating ubiquitous PGs are short and have a single or double side chain which lack an HA binding region. The presence of albumin in bone fluid is well established (Owen and Triffitt, 1976).

The dimensions of the anatomical structures illustrated (Figs 2–4) are average or composite values taken from Atkinson and Hallsworth (1982, 1983), Baud (1976), Cane *et al.* (1982), Jande (1971), Jande and Bélanger (1971), Knese (1979), Marotti (1980), Morris *et al.* (1982) and Palumbo (1986). Four fundamental lengths appear in Figs 2–4. One length is the center-to-center distance between two lacunae L (Fig. 2) and the second is the radius of curvature of the annulus b (Fig. 3). The other two fundamental

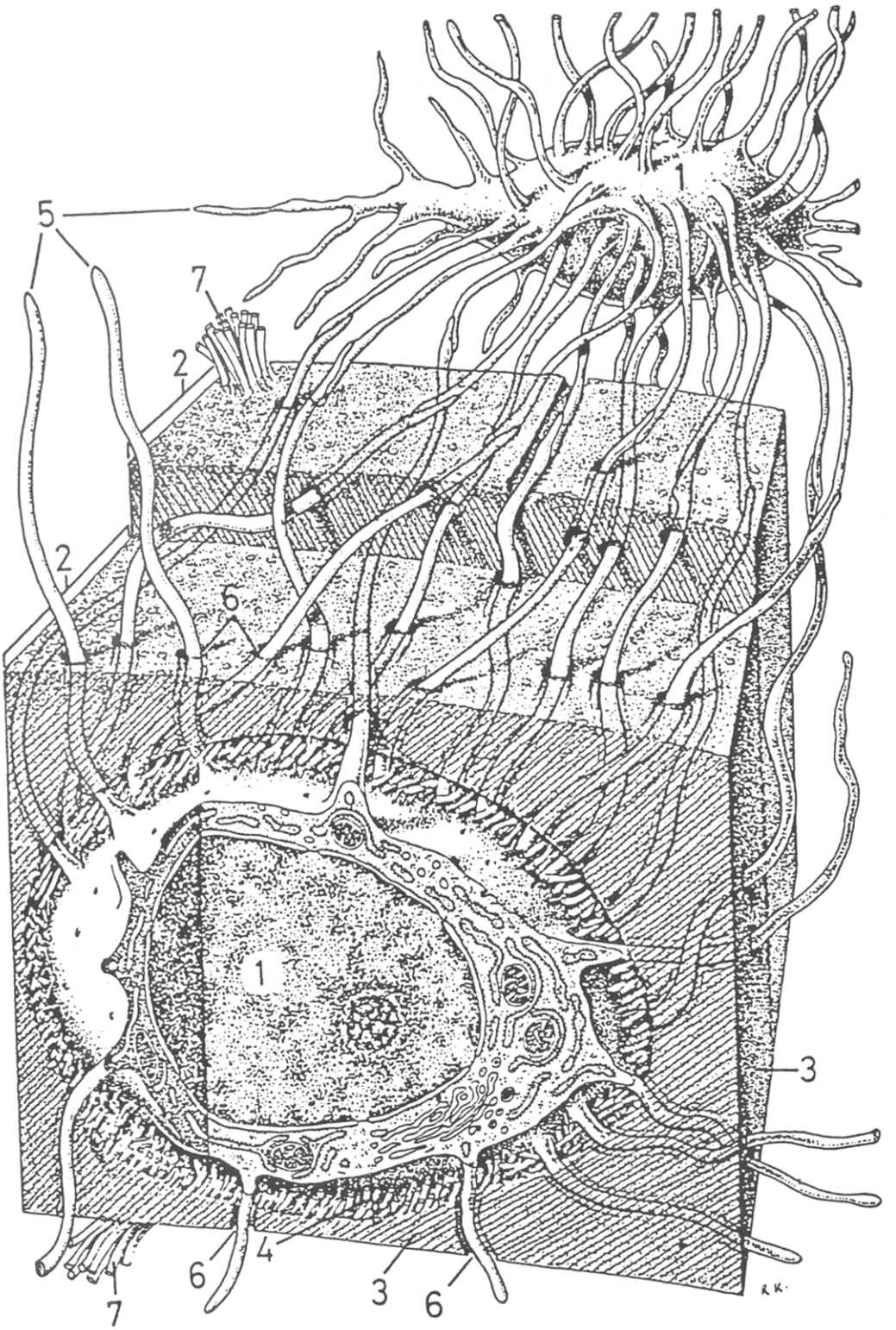

Fig. 1. Diagram of two osteocytes (1) in the lamellar bone of calcified bone matrix (3). Two neighboring lamellae (2) with different collagen fiber orientations (7) are visible. The osteocytic cell bodies are located in lacunae and are surrounded by a thin layer of uncalcified matrix (4). Their cell processes (5) are housed in canaliculi (6). Note that the gap junctions between the cell processes appear as a lap joint. From Krstic (1978), reproduced by permission from Springer.

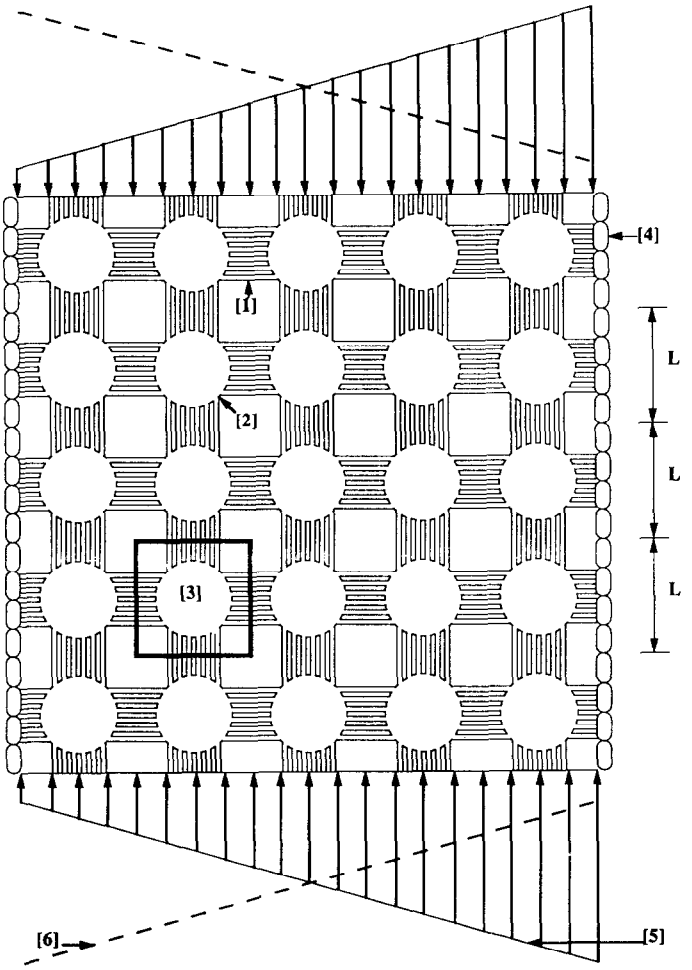

Fig. 2. An idealized model of a trabecular cross section illustrating the lacunar–canalicular porosity associated with the fluid space surrounding the osteocytes in a trabecula. The number (1) indicates one of the numerous canaliculi that connect lacunae (2). The number (1) also indicates the region of this figure that is enlarged many times in Fig. 3. Each lacuna (2) houses an osteocyte (not shown), and osteocytic processes (not shown) run from each osteocyte about half way down each canaliculus to connect, with a gap junction (not shown), to the osteocytic processes from the osteocyte housed in the adjacent lacuna. The number (3) indicates the periodic unit cell used in our calculation of the large-scale permeability constant k, (4) indicates bone cells on the surface of the trabecula. The linear stress distribution the trabecula is subjected to at one extreme of the cyclic loading is indicated by (5) and at the other extreme by (6). This linear stress distribution represents a periodic, combined axial and bending loading. The length L is the center-to-center distance between two lacunae. The material between the orthogonal sets of canaliculi (the regions appear as white squares on the figure) are regions of bone with the third level of porosity.

lengths (Figs 2 and 3) are the gap height of the annulus $(b-a)$ and the GAG spacing Δ.

Permeability constants

There are three permeability constants associated with the three hierarchical length scales Δ, $(b-a)$ and L. The three permeability constants are denoted by k_p, $k_{p,\text{eff}}$ and k, respectively, and each has the units of area. The local or small-scale permeability constant k_p represents the intrinsic permeability of the bone fluid flow through the GAG fibers and does not consider the boundaries of flow, namely, the surface of the cell process and the wall of the canaliculus. In order to account for the effect of these boundaries of the pore space, the effective permeability $k_{p,\text{eff}}$ constant is introduced. It represents an averaging of the small-scale permeability k_p over the annular pore space of the canaliculus. The large-scale permeability constant k represents the permeability of the entire canalicular system associated with each lacuna. The following items are discussed below in the order indicated: the largest scale constant k; then the smallest scale constant k_p; formulas for $k_{p,\text{eff}}$ and k; and the relationship of k_p to Δ.

The large-scale permeability constant $k=\kappa\mu$ is introduced as part of Darcy's law. If $\mathbf{u}$ represents the fluid velocity vector and ∇p the gradient of the pore

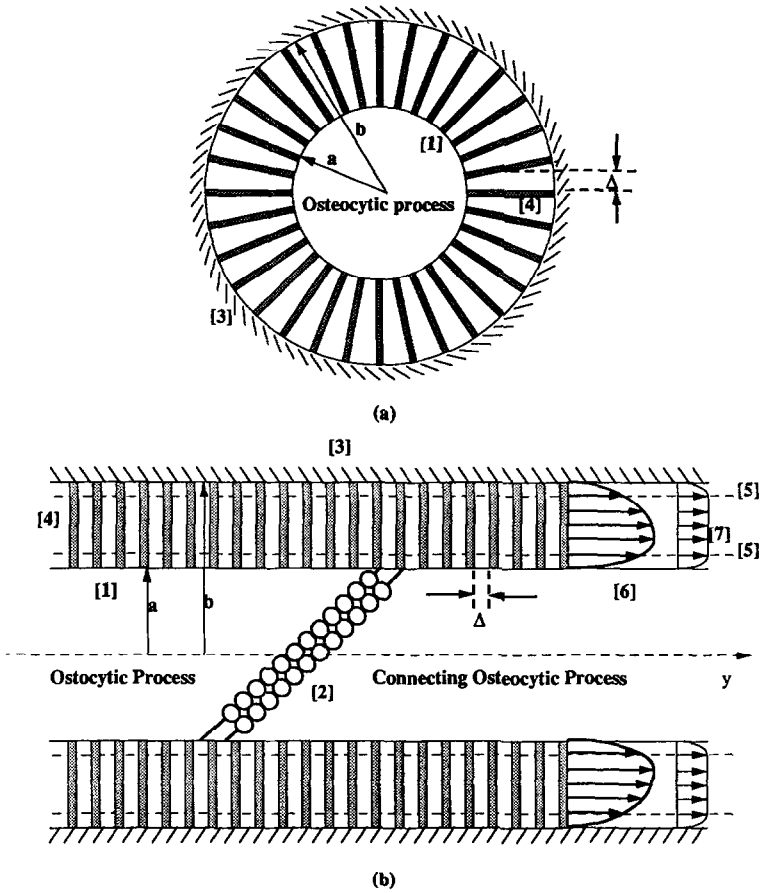

Fig. 3. An idealized model of the cross section of a canaliculus: (top) transverse cross section showing the annular shape of the region, (bottom) the longitudinal cross section. This figure is on a scale of about 1/500 times the scale of Fig. 2. This figure gives an enlarged view of a small central section of a typical canaliculus, such as the one labeled (1) in Fig. 2. The number (1) of this figure indicates the surface of the osteocytic cell membrane, (2) the gap junction between two connecting osteocytic cell processes, (3) the surface of the canalicular wall, (4) a typical fiber traversing the annular region and representing the cross linking proteoglycans. The dotted lines (5) represent the outer edge of the fiber induced boundary layer. The velocity distribution varies from a radially distorted parabola (6), to a plug flow (7) as the thickness of the fiber induced boundary layer diminishes due to an increase in the fiber density. Three of the four fundamental lengths that characterize the local fluid behavior are shown: the radius of curvature of the annulus b, the gap height of the annulus, $(b-a)$, and the open gap Δ between the fibers. The fourth fundamental length is the center-to-center distance length L between two lacunae shown in Fig. 2. While Fig. 2 is on the length scale L (approximately 35 μm) of the lacunar spacing, the field shown in Fig. 3 is $5L$ by $5L$ (175 μm by 175 μm); both panels of Fig. 3 are on a scale of about 1/500 that of Fig. 2, approximately 0.35 μm by 0.35 μm.

fluid pressure p, then Darcy's law is

$$\mathbf{u} = -\kappa \nabla p, \tag{1}$$

where the coefficient of permeability, $\kappa = k/\mu$, is a ratio of the permeability constant k to the fluid viscosity μ.

The local or small-scale permeability constant k_p for a fiber-filled medium is introduced as part of Brinkman's (1947) equation. The theory in Tsay and Weinbaum (1991) has shown that Brinkman's equation provides a highly accurate approximation for bounded flow in a channel with a fiber matrix provided the aspect ratio of the fibers is greater than five. This criterion for the aspect ratio is easily satisfied for long slender GAG fibers. We thus describe the fluid annulus surrounding the osteocytic process by a Brinkman equation for a fiber filled medium:

$$\nabla p = -\frac{\mu}{k_p}\mathbf{u} + \mu \nabla^2 \mathbf{u}. \tag{2}$$

Brinkman's equation (2) reduces to Darcy's law (1) in the dense fiber limit when k_p is small and to the standard Stokes equation (i.e. $\nabla p = \mu \nabla^2 \mathbf{u}$) in the limit where the fibers are dilute and k_p is large. If we require that the two terms on the right-hand side of equation (2) be of the same order, one can show through simple dimensional analysis that the thickness of the fiber induced boundary layer is of the order $\sqrt{k_p}$. The velocity profile in the annulus (Fig. 3b) and the shear stress at the surface of the cell process will depend on the relative thickness of the fiber induced boundary layer $\sqrt{k_p}$ compared to the width of the fluid annulus $(b-a)$.

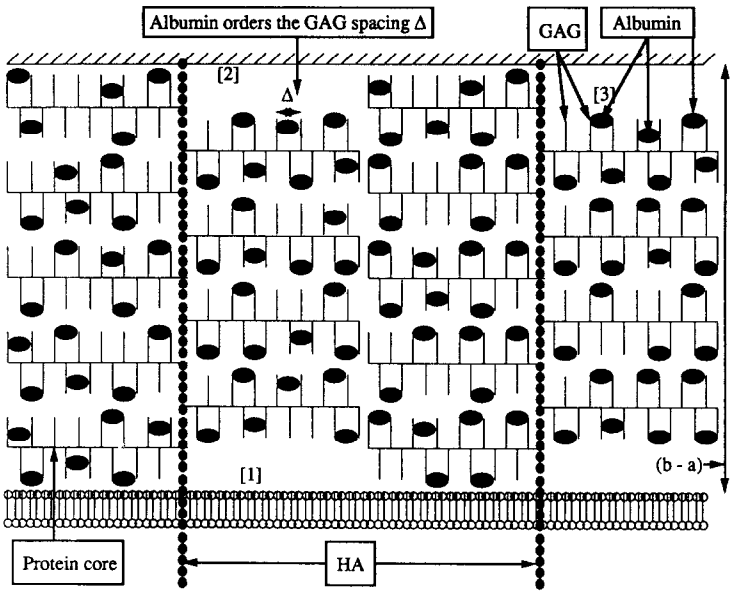

Fig. 4. An idealized model of the fiber matrix proteoglycan net in the annular region between the osteocytic cell membrane and the surface of the canalicular wall. This figure is on a scale of about 1/4 the scale of Fig. 3 and 1/2000 the scale of Fig. 2. This figure gives an enlarged view of the cross linking proteoglycan net in a small central section of a typical canaliculus, such as the one labeled [1] in Fig. 2. The number (1) of this figure indicates the osteocytic cell membrane, (2) the surface of the canalicular wall, and (3) the darkened ellipses represent albumin molecules. Two of the four fundamental lengths that characterize the local fluid behavior are shown: the gap height of the annulus $(b-a)$ and the open gap Δ between the fibers. This figure is modeled on fig. 2 of Curry (1986).

The average velocity of flow through a canalicular pore annulus containing the fiber matrix is obtained by dividing the volume flow rate Q through the canaliculus by the annular area $\pi(b^2-a^2)$. The effective permeability $k_{p,\text{eff}}$ is determined from the average velocity $Q/\pi(b^2-a^2)$, where Q is calculated from the solution of Brinkman's equation (2) for the velocity profile in the annulus. Q is related to the pressure gradient in the axial direction of a canaliculus by

$$k_{p,\text{eff}}=\frac{Q}{\pi(b^2-a^2)}\mu|\nabla p|^{-1}. \tag{3}$$

The large-scale permeability constant k is determined by first calculating the average tissue velocity u in the direction of a canaliculus. If n is an integer representing the number of canaliculi crossing each face of the periodic unit cell in Fig. 2 and L^2 is the area of the face of a periodic unit cell, then n/L^2 is the area surrounding each canaliculus and nQ/L^2 is the local average velocity u in the tissue. Darcy's law (1) can then be inverted to obtain an expression for the large-scale permeability constant k:

$$k=-\frac{\mu nQ}{L^2}|\nabla p|^{-1} \tag{4}$$

for the periodic unit cell illustrated in Fig. 2. We assume that the tissue is isotropic and thus n canaliculi cross the surface of the periodic unit cell in each of its three principal directions.

The value of the small-scale permeability constant k_p in equation (2) is for an infinite medium. It is a complicated function of the fiber spacing parameter Δ and the orientation of the flow relative to the fibers. A rigorous solution for the flow perpendicular to a two-dimensional square array of fibers is presented in Sangani and Acrivos (1982). This solution can be shown to be nearly independent of fiber orientation. A simple approximation to this solution is given in Tsay and Weinbaum (1991) which is accurate to within 10% for all fiber volume fractions less than 0.7:

$$k_p=0.0572a_0^2\left(\frac{\Delta}{a_0}\right)^{2.377}, \tag{5}$$

where a_0 is the fiber radius. A rough approximation to equation (5) is that k_p is approximately equal to the square of Δ; thus, since the Brinkman equation shows that the thickness of the fiber induced boundary layer is of the order $\sqrt{k_p}$, it follows that the boundary layer thickness is approximately equal to the fiber spacing parameter Δ. The lengths and permeability constants of this hierarchical model are summarized in Table 1.

Next, we wish to determine the relationship between the three permeability constants k_p, $k_{p,\text{eff}}$ and k. First, we derive an expression for k in terms of k_p. This is accomplished by solving the Brinkman equation (2) to determine the velocity profile in the canaliculus, integrating this velocity profile over the cross section to obtain the total flux Q and then substituting this result in formula (3) for k. Equation (2) applies in the cross section of an annular region (Fig. 3). The outer radius of this region is denoted by b and the inner radius by a; the ratio of b to a is denoted by q, $b=qa$.

The solution of equation (2) which satisfies the no-slip boundary conditions on the walls of the annulus is

$$u=\frac{k_p}{\mu}\frac{\partial p}{\partial y}\left[A_1 I_0\left(\gamma\frac{r}{b}\right)+B_1 K_0\left(\gamma\frac{r}{b}\right)-1\right], \quad (6)$$

where the y coordinate is along the axis of the annulus and

$$A_1=\frac{K_0(\gamma)-K_0(\gamma/q)}{I_0(\gamma/q)K_0(\gamma)-I_0(\gamma)K_0(\gamma/q)},$$

$$B_1=\frac{I_0(\gamma/q)-I_0(\gamma)}{I_0(\gamma/q)K_0(\gamma)-I_0(\gamma)K_0(\gamma/q)}. \quad (7)$$

Here K_0 and I_0 are modified Bessel functions of zeroth order and $\gamma=b/\sqrt{k_p}$ is a dimensionless length ratio.

Equation (6) can be integrated over the region $a\leqslant r\leqslant b$ to obtain the total flux Q through the annulus. This result is

$$Q=\frac{2\pi a^4 q^3}{\mu\gamma^3}\frac{\partial p}{\partial y}\left\{A_1[qI_1(\gamma)-I_1(\gamma/q)]\right.$$
$$\left.-B_1[qK_1(\gamma)-K_1(\gamma/q)]-\frac{\gamma(q^2-1)}{2q}\right\}. \quad (8)$$

Equations (6) and (8) can be written in much simpler form in the very dilute fiber limit where k_p becomes infinite. For this case, which we denote by the subscript ∞, equation (6) reduces to the solution of the Stokes equation for the flow in an annulus

$$u_\infty=\frac{a^2}{4\mu}\frac{\partial p}{\partial y}\left[\frac{r^2}{a^2}-1-\left(\frac{q^2-1}{\ln q}\right)\ln\frac{r}{a}\right], \quad (9)$$

and the volume flow rate Q_∞ in this limit is given by

$$Q_\infty=\frac{-\pi a^4}{8\mu}\left(\frac{\partial p}{\partial y}\right)\left[q^4-1-\frac{(q^2-1)^2}{\ln q}\right]. \quad (10)$$

Substitution of equation (8) into equation (4) yields the following expression for k:

$$k=\frac{2\pi n a^4 q^3}{\gamma^3 L^2}\left\{A_1[I_1(\gamma/q)-qI_1(\gamma)]\right.$$
$$\left.+B_1[qK_1(\gamma)-K_1(\gamma/q)]+\frac{\gamma(q^2-1)}{2q}\right\}, \quad (11)$$

and, since the quantity nQ/L^2 is equal to the average velocity u, the substitution of equation (9) into equation (4) yields k for the very dilute fiber matrix, which is denoted by k_∞,

$$k_\infty=\frac{n\pi a^4}{8L^2}(q^2-1)\left[q^2+1-\frac{(q^2-1)}{\ln q}\right]. \quad (12)$$

The decrease in the Darcy law permeability of the lacunar–canalicular system due to the fiber matrix, which is denoted by the ratio k/k_∞, is obtained from results (11) and (12),

$$\frac{k}{k_\infty}=\frac{16\left(\frac{q}{\gamma}\right)^3\left\{\frac{\gamma(q^2-1)}{2q}-A_1[qI_1(\gamma)-I_1(\gamma/q)]-B_1[K_1(\gamma/q)-qK_1(\gamma)]\right\}}{(q^2-1)\left[q^2+1-\frac{(q^2-1)}{\ln q}\right]}. \quad (13)$$

Another useful relationship between the permeability constants k_p and $k_{p,\mathrm{eff}}$ can be obtained by substituting equation (8) into the definition (3) of $k_{p,\mathrm{eff}}$:

$$\frac{k_{p,\mathrm{eff}}}{k_p}=\frac{2q}{\gamma(q^2-1)}\left\{\frac{\gamma(q^2-1)}{2q}-A_1[qI_1(\gamma)-I_1(\gamma/q)]\right.$$
$$\left.-B_1[K_1(\gamma/q)-qK_1(\gamma)]\right\}. \quad (14)$$

Equation (14) is a correction to k_p which takes into consideration the fiber induced fluid boundary layer at the boundaries of the annulus.

Shear stress at the surface of the osteocytic process

The shear stresses acting at the inner surface of the annular region, or the exterior surface of the membrane of the osteocytic process (see Fig. 3) is readily obtained from the gradient of the velocity profile (6) by evaluating it at $r=a$:

$$s(a)=\mu\frac{\partial u}{\partial r}(a)$$
$$=\frac{b}{\gamma}\frac{\partial p}{\partial y}[A_1 I_1(\gamma/q)-B_1 K_1(\gamma/q)]. \quad (15)$$

In the dilute fiber limit, equation (15) reduces to the inner wall shear stress for Stokes flow in an annulus, which we denote by $s_\infty(a)$,

$$s_\infty(a)=\mu\frac{\partial u}{\partial r}(a)=\frac{a}{2}\left(\frac{\partial p}{\partial y}\right)\left(1+\frac{1-q^2}{2\ln q}\right). \quad (16)$$

From equations (15) and (16), the ratio of the shear stresses on the osteocytic membrane when matrix components are present or absent in the annulus is given by

$$\frac{s(a)}{s_\infty(a)}=\left(\frac{2q}{\gamma}\right)\left[\frac{A_1 I_1(\gamma/q)-B_1 K_1(\gamma/q)}{1+\frac{1-q^2}{2\ln q}}\right]. \quad (17)$$

Evaluation of the magnitude of the shear stress must await a determination of the pressure gradient, which will be done in the next section. We will then return to the question of the magnitude of the shear stress on the osteocytic process in the sections titled Results and Discussion.

Fluid-saturated elastic porous media theory

Next, we wish to establish the relationship between large-scale deformation of the tissue and small-scale fluid mechanisms described in the two previous sections. In this way, we will relate the externally applied loads to the fluid shear stress at the cell membrane surface. The stress-induced flow of the interstitial fluid at the level of the large-scale permeability k is considered using the poroelasticity model.

Table 1. A list of the length scales and the permeability constants associated with the various length scales

	Length scale	Permeability constant
Lacunar-canalicular system level	L = the center-to-center distance between two lacunae (approximately 35 μm.).	k = large or lacunar scale
Canaliculus level	a = the radius of the cell process (approximately 0.1 μm.). b = the radius of the annulus (approximately 0.2 μm.). $(b-a)$ = the gap height of the annulus (approximately 0.1 μm.).	$k_{p,\mathrm{eff}}$ = the effective or average of the small scale
Canalicular pore contents level	Δ = the open gap between the fibers (approximately 7 nm.). a_0 = the fiber radius (0.6 or 2 nm). $\sqrt{k_p}$ = the thickness of the fiber induced boundary layers; $\sqrt{k_p} \approx \Delta$.	k_p = local or small scale

At the large-scale level, we employ the theory of stress-induced flow of interstitial fluid in porous solids. This theory, which originated in the geomechanics literature, is primarily due to Biot [see Biot (1941), Biot and Willis (1957) and Rice and Cleary (1976)], and is often called *poroelasticity* or *Biot theory*. The theory has been applied to bone tissue by Nowinski and Davis (1970, 1972), Johnson *et al.* (1982), Johnson (1984) and, more recently, by Williams (1992). The theory has two basic assumptions: (i) Darcy's law governs the flow of the interstitial fluid, (ii) the matrix material of the porous medium follows Hooke's law. Our brief summary of the theory follows the presentation of Rice and Cleary (1976). One of the differential equations governing the pore fluid pressure p is

$$c\nabla^2\left(T_{kk}+\frac{3}{B}p\right)=\frac{\partial}{\partial t}\left(T_{kk}+\frac{3}{B}p\right), \tag{18}$$

where the coefficients c and B are given by

$$c=\kappa\left[\frac{2G(1-\nu)}{(1-2\nu)}\right]\left[\frac{B^2(1+\nu_u)^2(1-2\nu)}{9(1-\nu_u)(\nu_u-\nu)}\right],$$

$$B=\frac{\dfrac{1}{K}-\dfrac{1}{K_s}}{\dfrac{\nu_0}{K_f}+\dfrac{1}{K}-\dfrac{(1+\nu_0)}{K_s}}, \tag{19}$$

respectively. In equation (18), T_{kk} represents the sum of all the normal stresses on three perpendicular planes in the porous medium and includes the stresses in the solid matrix and the pore water pressure. In formula (19), $K=2G(1+\nu)/3(1-2\nu)$ is the 'drained' bulk modulus (i.e. the bulk modulus of the solid at constant pore pressure p), K_s is the bulk modulus of the solid phase, K_f is the bulk modulus of the fluid and ν_0 is the value of the fluid volume fraction in the unstressed reference state. The stress T_{kk} and the pressure p must also satisfy

$$\nabla^2\left(T_{kk}+\frac{6(\nu_u-\nu)p}{B(1-\nu)(1+\nu_u)}\right)=0, \tag{20}$$

which comes from the compatibility condition on the strain in the solid matrix.

The values of the coefficients appearing in equations (18) and (20) are described here. The bulk modulus K_f for salt water is given in *Marks' Handbook for Mechanical Engineers* as 2.3 GPa. The value of K is determined from the measured values of Young's modulus and Poisson's ratio reported in Cowin (1989) as 14 GPa. A value for the fluid volume fraction in the unstressed reference state, ν_0, is taken from experimental data reported by Morris *et al.* (1982). These authors estimate that the fluid volume associated with lacunar–canalicular extracellular bone fluid is 0.05 ml/ml, thus we take $\nu_0=0.05$. As we were unable to find any data on the bulk modulus of the solid phase K_s, we estimated it to be 20 GPa. As K_s must be greater than K, it appears not unreasonable to assume it to be about 25 to 50% larger. The coefficient B for bone is then found, by equation (19), to be 0.53. From the literature concerning the experimentally measured values of the elastic constants of bone, e.g. Cowin (1989), the value of the drained shear modulus G of bone is about 6 GPa and the value of the drained Poisson's ratio ν of bone is about 0.25. As we were unable to find any data on the undrained Poisson's ratio ν_u of bone, $0.5 \geqslant \nu_u \geqslant \nu$, we have estimated that it is about 0.3. Using these numbers and our estimate of B, 0.53, c from equation (19) is given by κ (13.5 GPa). This value corresponds to $K_s=1.43K$, c varies from κ(8.84 GPa) to κ(14.9 GPa) as K_s is varied from $1.25K$ to $1.5K$.

Because of the relatively low lacunar–canalicular porosity, the solid matrix supports most of the mechanical load applied to the bone, and the pore pressure supports only a small portion of the load. The value of the factor multiplying the pressure in the compatibility equation (20) is approximately 0.56, based on the above data and estimates in the paragraph above. Since the pore pressure p is much less than the stress T_{kk}, the term containing pressure in equation (20) is neglected in this analysis, and equation (20) reduces to the condition that $\nabla^2 T_{kk}=0$. Equation (18), with the stress T_{kk} satisfying the condition $\nabla^2 T_{kk}=0$, is employed in the next section to determine the pore pressure from the mechanical loads applied to the whole bone.

The fluid pressure in the osteocytic pore space

The solution of the boundary value problem to determine the fluid pressure in the osteocytic pore

space is outlined here. Equation (18) of the poroelastic theory is employed to relate the pore pressure to the externally applied loads. In the Results section we shall use a solution to this equation for the pore pressure to estimate the maximum shear stress on the osteocytic process.

As a model for calculating the local fluid pressure gradient in the canaliculus from the external load, we consider the idealized trabecular section of uniform width shown in Fig. 2. Our idealized model is a one-dimensional slab of a thickness $2d$, which lies in the region $-d \leqslant y \leqslant d$, and has large dimensions in both the x and z directions. The actual length dimensions in the x and z directions do not enter the problem as we are considering a loading that is a combination of an axial load and a pure bending moment about the x axis perpendicular to the plane of the diagram. The only nonzero, stress is the applied stress in the z direction, T_{zz}, thus $T_{kk}=T_{zz}$. From the fact that the loading is an applied cyclic bending and axial loading and the compatibility condition $\nabla^2 T_{kk}=0$, it follows that T_{zz} may be represented by

$$T_{zz}=-\sigma_0-\left(\sigma+\frac{m}{I}y\right)\sin\omega t, \tag{21}$$

where σ_0, σ, m/I are constants and the loading period is $2\pi\omega^{-1}$. This stress distribution is illustrated in Fig. 2. The term $-\sigma_0$ represents a constant axial compressive stress, the term $\sigma\sin\omega t$ represents a sinusoidally time-varying axial compressive stress, and $(m/I)y\sin\omega t$ represents a sinusoidally time-varying axial bending stress where m is the applied moment and I can be considered to be the area moment of inertia per unit length of the cross-sectional area of the slab. The thickness $2d$ can be selected to represent either the thickness of a trabecula, or the thickness of the bone specimen in the four-point bending apparatus experiments.

Placing the formula (21) for T_{zz} in equation (18), and noting that all other stress components are zero, the partial differential equation for the pore pressure is

$$c\frac{\partial^2 p}{\partial y^2}-\frac{\partial p}{\partial t}=-\frac{B\omega}{3}\left(\sigma+\frac{m}{I}y\right)\cos\omega t, \tag{22}$$

or

$$\frac{\partial P}{\partial\tau}-\frac{\partial^2 P}{\partial Y^2}=(1+MY)\cos T\tau, \tag{23}$$

where we have introduced the following dimensionless quantities:

$$Y=\frac{y}{d},\quad \tau=\frac{ct}{d^2},\quad P=\frac{3p}{\sigma BT},\quad T=\frac{\omega d^2}{c},\quad M=\frac{md}{\sigma I}. \tag{24}$$

The first three of the dimensionless quantities introduced in equation (24) render the length, time and pressure variables dimensionless. In addition, two important dimensionless parameters, M and T, are introduced in equation (24). The dimensionless quantity M is a ratio of the applied bending load to the applied axial load, M is equal to zero when there is axial loading, but no bending, and M becomes infinite when there is bending but no axial loading. The dimensionless quantity T is the ratio of the characteristic time of relaxation of the fluid pore pressure, $\tau_r=d^2c^{-1}$, to the characteristic time of applied forcing, $\tau_f=\omega^{-1}$; T is small when $\tau_r \ll \tau_f$ and large when the reverse is true. The characteristic time of relaxation of the fluid pore pressure, $\tau_r=d^2c^{-1}$, is related to the small-scale permeability constant k_p through the formula for k given by equation (11), and the formula for c given by (19),

$$\tau_r=\frac{\mu d^2\left\{\dfrac{(1-2\nu)9(1-\nu_u)(\nu_u-\nu)}{[2G(1-\nu)][B^2(1+\nu_u)^2(1-2\nu)]}\right\}}{2\pi n a(k_p)^{3/2}\left\{A_1[I_1(\gamma/q)-qI_1(\gamma)]+B_1[qK_1(\gamma)-K_1(\gamma/q)]+\dfrac{\gamma(q^2-1)}{2q}\right\}}. \tag{25}$$

In the previous section, it was shown that $c=\kappa(13.5\text{ GPa})$; thus from equation (19), the term in brackets in the numerator of equation (25) has the value $(13.5\text{ GPa})^{-1}$.

The boundary condition used for the solution of equation (23) is

$$\frac{\partial P}{\partial Y}\pm\eta P=0,\quad \text{at } Y=\pm 1, \tag{26}$$

where η is a constant representing fluid leakage at the free surface that is proportional to the instantaneous excess pore pressure there. At one extreme ($\eta=0$, $\partial P/\partial Y=0$) the wet bone surface at $Y=\pm 1$ is in a humidity chamber where the fluid is not free to drain at the free fluid–air interface because of the pore fluid surface tension. At the other extreme ($\eta\to\infty$, $P=0$), the wet bone surface at $Y=\pm 1$ has free drainage at the boundaries. In between, measured by other values of η, there is leakage, which is a combination of some pores being able to drain freely and others being held at the free fluid–air interface because of the pore fluid surface tension. Thus, one can view η as a boundary leakage coefficient, $\eta=0$ corresponding to no leakage and $\eta\to\infty$ to free flow. The boundary conditions associated with $\eta=0$ and $\eta\to\infty$ are discussed by Johnson *et al.* (1982). The boundary condition ($\eta=0$, $\partial P/\partial Y=0$) was employed by Johnson *et al.* (1982) and Salzstein *et al.* (1987). The solution of (23) subject to

the more general boundary condition (26) is

$$P(Y,\tau)=\frac{1+MY}{T}\sin T\tau-\frac{1}{T}\mathrm{Im}\left[\left(\frac{M(1+\eta)\sinh\beta Y}{\beta\cosh\beta+\eta\sinh\beta}+\frac{\eta\cosh\beta Y}{\beta\sinh\beta+\eta\cosh\beta}\right)e^{iT\tau}\right], \tag{27}$$

where $\beta=(1+i)\sqrt{T/2}$. For the boundary condition $P=0$ ($\eta\to\infty$) at $Y=\pm1$, equation (27) reduces to

$$P(Y,\tau)=\frac{1+MY}{T}\sin T\tau-\frac{1}{T}\mathrm{Im}\left[\left(\frac{M\sinh\beta Y}{\sinh\beta}+\frac{\cosh\beta Y}{\cosh\beta}\right)e^{iT\tau}\right], \tag{28}$$

while for the boundary condition $\partial P/\partial Y=0$ ($\eta=0$) at $Y=\pm1$, equation (27) becomes

$$P(Y,\tau)=\frac{1+MY}{T}\sin T\tau-\frac{M}{T}\mathrm{Im}\left[\left(\frac{\sinh\beta Y}{\beta\cosh\beta}\right)e^{iT\tau}\right]. \tag{29}$$

The model employed above for calculating the local fluid pressure from the external load was a plate-like structure of uniform width, bent about its most flexible direction. In this paper, this model will be used for two different physical situations. The first situation is an *in vivo* model for a trabecula. For a trabecula $d=100$ μm and the boundary condition $P=0$ ($\eta\to\infty$) at $Y=\pm1$ is employed. This plate-like shape and loading also corresponds to the specimen shape and loading employed in the four-point SGP bending experiments reported by Salzstein *et al.* (1987) and Scott and Korostoff (1990). This is the second situation in which the model will be employed. For these bending experiments $d=0.5$ mm and the no-leakage boundary condition $\partial P/\partial Y=0$ ($\eta=0$) at $Y=\pm1$ is appropriate.

RESULTS

Our result concerning the effect of the wall of the canaliculus on the small-scale permeability is illustrated (Fig. 5) by plots of the expressions (13) and (14) for the ratios k/k_∞ and $k_{p,\mathrm{eff}}/k_p$ against the dimensionless length parameter $\alpha=(b-a)/\sqrt{k_p}$ for $q=1.1$, 2.0, 5.0, 10. Note that the width of the fluid layer $(b-a)$, rather than the canalicular radius b, is the characteristic length of the fluid flow domain. For this reason, the parameter α $[\alpha=(b-a)/\sqrt{k_p}]$, rather than γ $(\gamma=b/\sqrt{k_p})$, will be used in plotting all the results in this paper, although the formulas can be more compactly written using γ. One of the remarkable results

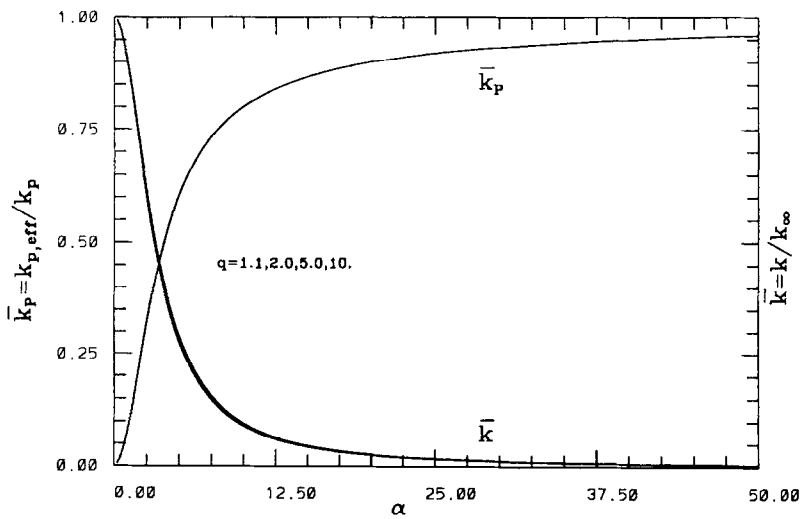

Fig. 5. Plots of the ratios $k_{p,\mathrm{eff}}/k_p$ and k/k_∞. The plot of equation (14) for the ratio $k_{p,\mathrm{eff}}/k_p$ against the dimensionless length parameter α $[\alpha=(b-a)/\sqrt{k_p}$ and related to γ in (14) by $\gamma=\alpha q/(q-1)]$ for $q=1.1$, 2.0, 5.0, 10. The curves for these four values of q cannot be distinguished on the scale of the figure and appear as a single curve. The quantity $k_{p,\mathrm{eff}}/k_p$ is a ratio of the small scale permeability constants, the effective permeability $k_{p,\mathrm{eff}}$ (accounts for the presence of the walls of the annulus) and the infinite medium Darcy law permeability constant k_p that appears in equation (2). Also there are plots of equation (13) for the ratio k/k_∞, against the dimensionless length parameter α $[\alpha=(b-a)/\sqrt{k_p}$ and related to γ in equation (13) by $\gamma=\alpha q/(q-1)]$ for $q=1.1$, 2.0, 5.0, 10. Although there are actually four curves for the values of q indicated, they are nearly indistinguishable on the scale of the figure. The ratio k/k_∞ is the ratio of the lacunar–canalicular porosity scale permeability constant k for channels filled with transverse fibers to the lacunar–canalicular porosity scale permeability constant k_∞ for channels with no transverse fibers.

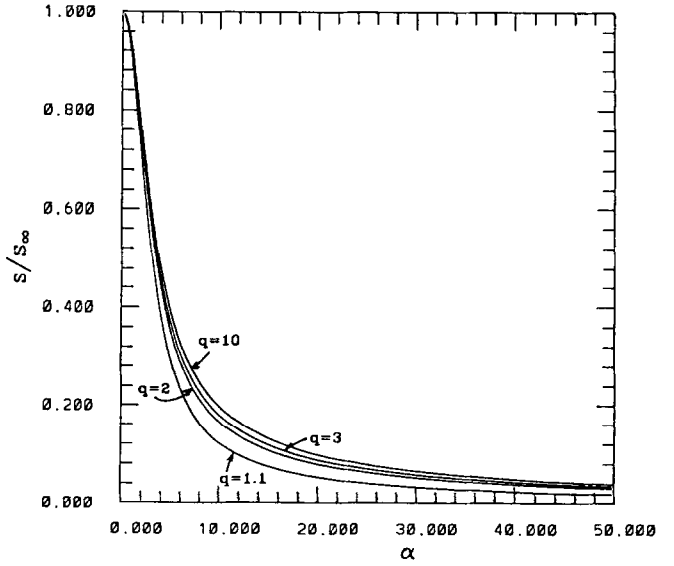

Fig. 6. A plot of equation (17) for the shear stress ratio $s(a)/s_\infty(a)$ against the dimensionless length parameter α [$\alpha=(b-a)/\sqrt{k_p}$ and related to γ in equation (17) by $\gamma=\alpha q/(q-1)$] for $q=1.1$, 2.0, 3.0, 10. The ratio $s(a)/s_\infty(a)$ is the ratio of the shear stress on the osteocytic membrane when channels are filled with transverse fibers to the shear stress when the channels are free of fibers. Note this ratio is independent of the loading (pore pressure gradient).

discovered in plotting $k_{p,\text{eff}}/k_p$ and k/k_∞ (Fig. 5) was that both families of curves are nearly independent of q. The differences for $2.0 \leqslant q \leqslant 3.0$, the anticipated physiological range, could not be distinguished on the scale of the curves (Fig. 5). The effective permeability of the canaliculi containing the fiber matrix, $k_{p,\text{eff}}$, and the lacunar–canalicular scale permeability constant of the bone, k, are therefore nearly independent of the ratio of the radii of the inner and outer boundaries of the annulus.

The effect of the fiber matrix on the shear stress ratio is illustrated by the plots (Fig. 6) of $s(a)/s_\infty(a)$, as given by equation (17), against the dimensionless length parameter $\alpha=(b-a)/\sqrt{k_p}$. The variation of $s(a)/s_\infty(a)$ with q is again very small for $q>2$, but there are more significant variations as q is further decreased in contrast to the results for the permeability ratios (Fig. 5). The plots (Fig. 6) of equation (17) are for the same values of q employed in the plots of $k_{p,\text{eff}}/k_p$ and k/k_∞ (Fig. 5). More significant variations are to be expected for the shear stress ratio (Fig. 6), as opposed to the permeability ratios (Fig. 5), as q is increased since the permeability is an average property of the annulus, whereas the shear stress at $r=a$ reflects the local behavior in the boundary layer. One observes that the primary decrease in $s(a)/s_\infty(a)$ occurs for $\alpha<10$. For the conditions $\alpha\cong 40$ and $q<3$, which our interpretation of the theory suggests correspond to physiological conditions, $s(a)/s_\infty(a)<0.05$.

The effect of the geometry of the canaliculus and the fiber matrix on the pore fluid pressure relaxation times is illustrated (Fig. 7) by plots of the log of the fluid pore pressure relaxation time, $\tau_r=d^2c^{-1}$, given by equation (25), against the dimensionless length parameter α for different values of q (1.5, 2.0, 2.5, 3.0, 5.0) and for $2d=1$ mm. This value of d corresponds to the *in vitro* experimental situations of Salzstein and Pollack (1987) and of Scott and Korostoff (1990). Anatomical studies cited in the section on model development suggest that the most likely range of q is between 2.0 and 3.0. On the basis of anatomical data from these same references, the values of b and n were selected as $b=200$ nm and $n/L^2=20/(35\ \mu\text{m})^2$. The viscosity of water μ is 10^{-2} dyn s $(\text{cm})^{-2}=1\times10^{-3}$ Pa s $=1\times10^{-12}$ GPa s. Note that the same value of τ_r can be obtained with different combinations of values of q and L (Fig. 7). The choice of q and α will be more critically analyzed in the Discussion section.

The transverse distribution of the pore pressures (Fig. 8) are shown at 45° increments in phase obtained from equations (28) and (29) for $M=10$ and three values of T. Three values of the dimensionless time parameter T are the two limiting values $T=0.01$ and $T=100$, and the anticipated normal value $T=1$. For $T=0.01$ the fluid pore pressure relaxation time, $\tau_r=d^2c^{-1}$, is short compared to the period of the loading cycle, $\tau_f=\omega^{-1}$; for $T=1$, τ_r and τ_f are comparable and when $T=100$, τ_f is short compared to τ_r. A value of $M=10$ was selected to represent the situation one would expect in the long bones of the leg during locomotion, where bending dominates. The solution for the wetted boundary condition ($P=0$ ($\eta\to\infty$) at $Y=\pm1$) associated with the *in vivo* trabecula is shown in Fig. 8(a)–(c). The solution for the no-leakage boundary condition ($\partial P/\partial Y=0$ ($\eta=0$) at $Y=\pm1$) associated with the *in vitro* experimental situations of Salzstein and Pollack (1987) and Scott

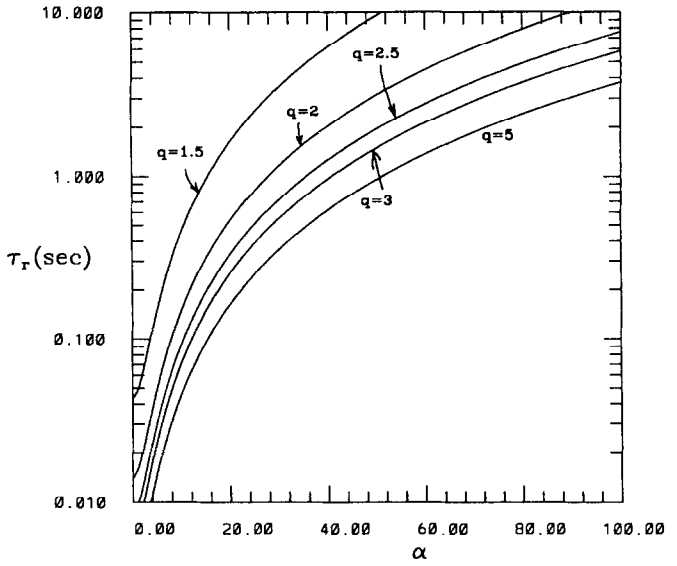

Fig. 7. A plot of the log of the pore fluid pressure relaxation time, $\tau_r = d^2 c^{-1}$ ($d = 0.5$ mm) against the dimensionless length parameter α [$\alpha = (b-a)/\sqrt{k_p}$] for $q = 1.5, 2.0, 2.5, 3.0, 5.0$. This is a plot of equation (25) using expression (11) for the reduction in the large scale permeability constant k due to the fiber-matrix parameter α. The values for the parameters employed were $b = 200$ nm, $n/L^2 = 20/(35\ \mu\text{m})^2$ and μ was taken to be the viscosity of water.

and Korostoff (1990) is shown in Fig. 8(d)–(f). These curves depend upon the width dimension d only through the dimensionless numbers T, M, Y and τ, but not the dimensionless pressure P. Observe that the scales for the dimensionless pressure in Fig. 8(a) and (d) are considerably different. One can see that the no-leakage boundary condition employed for Fig. 8(d) leads to considerable buildup of pressure at small values of the dimensionless frequency ratio T. The small asymmetry of the pore pressure distribution about $Y = 0$ in Fig. 8 is due to the small axial load.

The maximum shear stress on the membrane surface $r = a$ of the osteocytic processes in a trabecula (*in vivo*) during a loading cycle is determined by combining equations (15) and (28). Formula (15) gives the shear stress on the membrane surface of the osteocytic processes in terms of the pressure gradient, and formula (28) provides the dimensionless pressure distribution in the domain of interest for the boundary condition $P = 0$ ($\eta \to \infty$) at $Y = \pm 1$. This boundary condition is the appropriate one for an *in vivo* situation in which the surface of the trabecula is a porous fluid filled phase. The maximum shear stress at any position Y on the membrane surface during the course of one temporal cycle, which we denote by $s_{\max}$, is given by

$$s_{\max} = \max \left[\frac{MBb\sigma}{3\gamma d} [A_1 I_1(\gamma/q) - B_1 K_1(\gamma/q)] \operatorname{Im}\{W(Y) e^{iT\tau}\} \right]_Y, \quad (30)$$

where Y is held fixed and

$$W(Y) = U(Y) + iV(Y) = 1 - \beta \left(\frac{\cosh \beta Y}{\sinh \beta} + \frac{\sinh \beta Y}{M \cosh \beta} \right). \quad (31)$$

A simple analytic expression for $s_{\max}$ cannot be obtained since the arguments of the functions in equation (30) are complex. However, note that if we introduce the definition

$$f(Y, \tau) \equiv \operatorname{Im}\{W(Y) e^{iT\tau}\} = U(Y) \sin T\tau + V(Y) \cos T\tau, \quad (32)$$

where $W(Y) = V(Y) + iU(Y)$, $f(Y, \tau)$ has a maximum in τ at constant Y for

$$T\tau_{\max} = \tan^{-1} \frac{U}{V} + N\pi, \quad (33)$$

where N is an integer. $\tau_{\max}$ therefore indicates the time in the cycle at which this maximum occurs at any position Y. The right-hand side of equation (33) is a function of Y for a given value of M. By choosing $N = 0$ and letting U and V be greater than or less than zero in the complex plane, $V + iU$, one can obtain solutions for $T\tau_{\max}$ which lie in the range 0–2π. If equation (33) is substituted in equation (32), one finds that at $\tau_{\max}$, $f(Y, \tau)$ has the value $f(Y, \tau_{\max}) = |W| = \sqrt{U^2 + V^2}$. The function $|W|$, which is proportional to the absolute value of the shear stress $s_{\max}$, is plotted in Fig. 9. An interesting change in behavior is observed as M is increased. For $M \ll 1$, $s_{\max}$ is symmetric about $Y = 0$, where the shear stress vanishes, as one would anticipate for a pure axial load. For $0 \leqslant M \leqslant 3$, there is a single nodal point for vanishing shear stress and the maximum shear stress

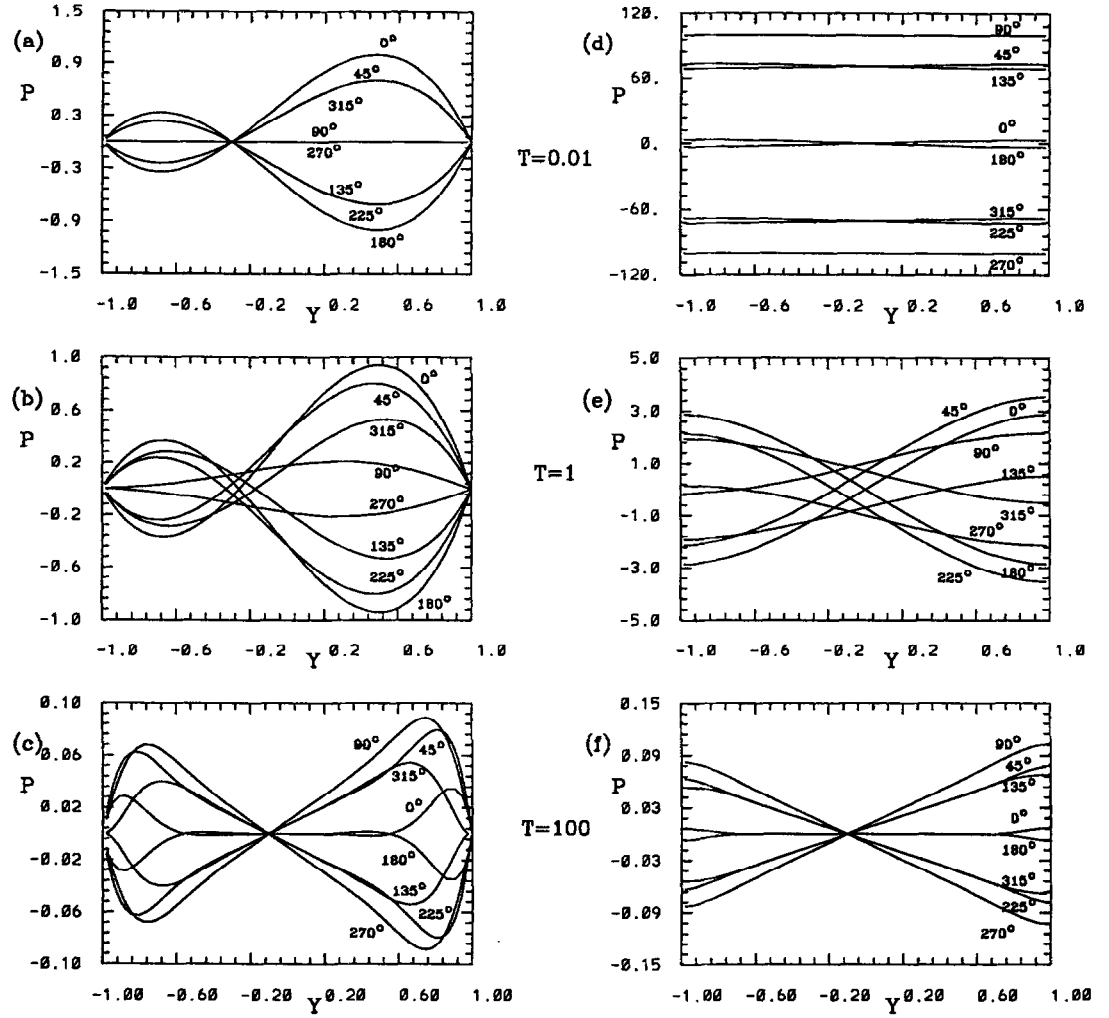

Fig. 8. (a, b, c) Plot of the solutions for the dimensionless excess fluid pressure P in equation (28) for the boundary condition $P=0$ $(\eta\to\infty)$ at $Y=\pm 1$, as a function of the dimensionless distance Y across a bone sample at 45° increments in phase. The curves are plotted from equation (28) for three values of T: (a) $T=0.01$; (b) $T=1$; (c) $T=100$, and $M=10$, a value of M where one would expect bending to dominate. (d, e, f). Plot of the solutions for the dimensionless excess fluid pressure P in equation (29) for the boundary condition $\partial P/\partial Y=0$ $(h=0)$ at $Y=\pm 1$, as a function of the dimensionless distance Y across a bone sample at 45° increments in phase. The curves are plotted from equation (29) for three values of T: (d) $T=0.01$; (e) $T=1$; (f) $T=100$, and $M=10$. These curves depend upon the width dimension d only through the dimensionless numbers T, M, Y and τ, but not the dimensionless pressure P.

distribution becomes increasingly asymmetric as M is increased. At $M=3$, a second nodal point develops at the left-hand boundary, which then moves inward as M increases. Finally for $M\gg 1$ the $|f(Y,\tau_{max})|$ distribution again becomes symmetric. The maximum stress throughout the specimen for any M occurs at $Y=1$, except for the limiting cases $M=0$ and $M=\infty$ where the solution is symmetric.

The fiber spacing Δ can be related to q and α (Fig. 10) and the curves in Fig. 10 used in combination with those in Fig. 7 to check the reasonableness of our assumption that the GAG is ordered by albumin and Δ is approximately 7 nm. Using the approximate formula (5) for k_p and the definition of $\alpha=[(b-a)/\sqrt{k_p}]$, one can rewrite equation (5) as

$$\Delta=(a_0)^{0.1586}\left[\frac{b(q-1)}{0.2391\alpha q}\right]^{0.8414}. \tag{34}$$

The curves in Fig. 10 are a plot of equation (34) where b is the radius of the canaliculus and a_0 the radius of the fiber. Two types of fibers have been suggested to exist in aqueous solutions, very slender fibers of approximately 0.6 nm radius associated with GAG side-chains and 2 nm radius fibers associated with a typical protein core of a PG. We assume here that the very slender fibers of 0.6 nm radius associated with the GAGs are principal occupants of the pore fluid space in the canaliculi because they are the most numerous fibers and provide the greatest fiber length (Fig. 4). If we now choose $q=2.8$, a value in the

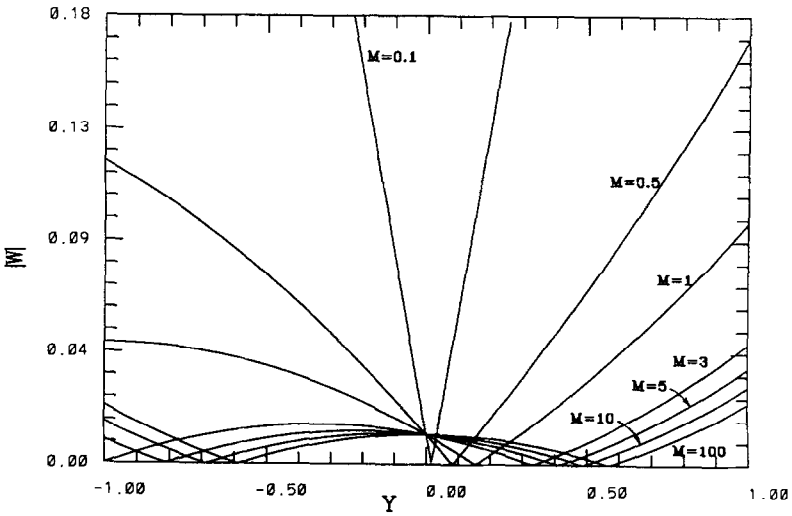

Fig. 9. Profiles of the function $|W| = \sqrt{U^2 + V^2}$ across a trabecular element for different values of M. The function W is given by equation (31) and its absolute value is proportional to the maximum shear stress s_{max} on the membrane surface of the osteocytic processes during the loading cycle. The time at which this maximum occurs for any Y is given by equation (32).

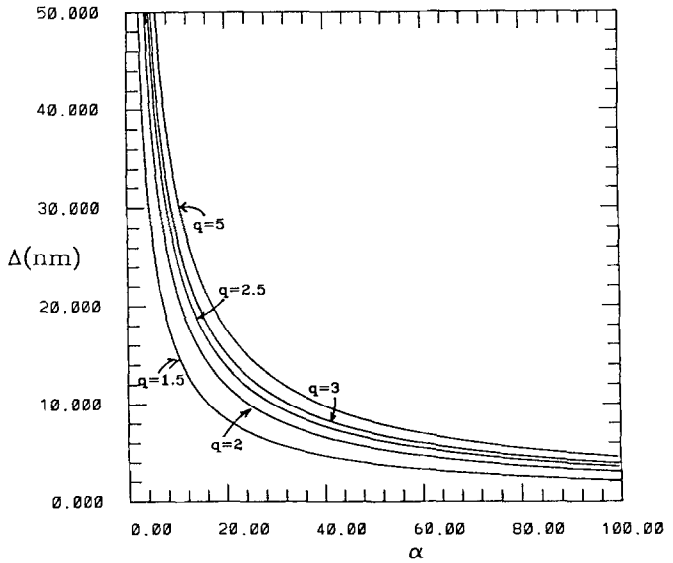

Fig. 10. A plot of the fiber spacing parameter Δ (open gap between fibers) against the dimensionless length parameter α [$\alpha = (b-a)/\sqrt{k_p}$] for $q = 1.5, 2.0, 2.5, 3.0, 5.0$. The value of a_0 was taken to be 0.6 nm, that of b to be 0.2 μm.

physiological range $2.0 < q < 3.0$, and require that the pore relaxation time τ_r be 2 s, the measured value in Salzstein and Pollack (1987), one finds (Fig. 7) that α is 37.7. For this value of α and $q = 2.8$, one observes (Fig. 10) that Δ is 7.0 nm. We have actually calculated Δ for the entire physiological range of q from 2.0 to 3.0 and found that Δ varies between 7 and 9 nm. This indicates that the solution for Δ is not sensitive to the exact geometry of the osteocytic process in the canaliculus. The solution for Δ is thus very close to 7 nm for all reasonable canalicular geometries.

The magnitude of the maximum shear stress on the membrane surface of the osteocytic processes in a trabecula (*in vivo*) during a loading cycle (Fig. 11) can be calculated from equations (30)–(33) and compared with the shear stress levels at which the release of intracellular Ca^{2+} and second messengers are observed to occur. In Fig. 11 the maximum dimensional shear stress is plotted as a function of M at several positions within the trabecula. These calculations assume that the thickness $2d$ of the trabecula is 200 μm, $b = 200$ nm, $n/L^2 = 20/(35\ \mu\text{m})^2$, $q = 2.8$, $\alpha = 51$ and μ is

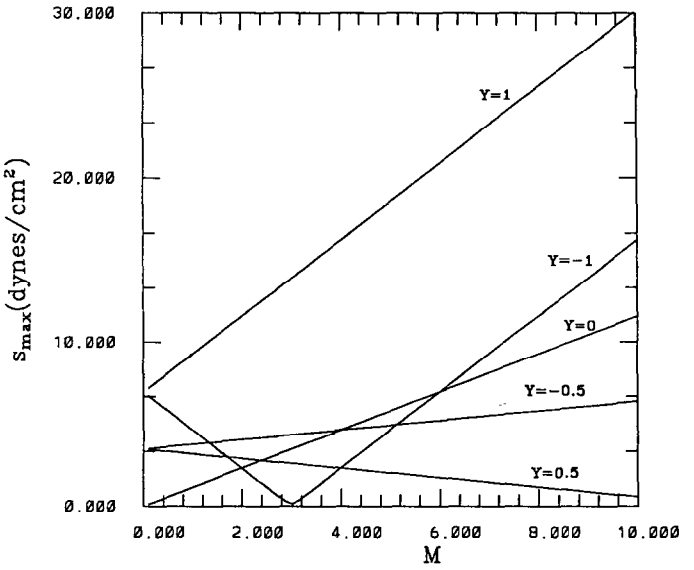

Fig. 11. A plot of the maximum shear stress s_{max} on the membrane surface of the osteocytic processes, as a function of the applied bending to axial load ratio M, at different locations Y within the trabecular element for *in vivo* conditions, $P=0$ at $Y=\pm 1$. The results are for the model of a trabecula. The values for the parameters employed were: trabecular thickness $2d=200\ \mu m$, $\sigma=2\times10^7$ dyn cm^{-2}, $b=200$ nm, $n/L^2=20/(35\ \mu m)^2$, $\tau_r=0.0724$ s, $q=2.8$, $\alpha=51$ and μ was taken to be the viscosity of water.

equal to the viscosity of water. The value of pore fluid pressure relaxation time τ_r for a trabecula with this microstructure and thickness is 0.0724 s. Thus, if the period of the forcing is 1 s, $T=0.0724$. When $M=1$ the maximum shear stress on the osteocytic process at the trabecular surface $Y=1$ is about 8 dyn cm^{-2} if a representative axial load of 2×10^7 dyn cm^{-2} is applied at 1 Hz. This will increase to about 30 dyn cm^{-2} when M is increased to 10. The fluid shear stresses on the membranes of the osteocytic processes in the canaliculi are roughly six orders of magnitude smaller than the fluid pressure, but lie precisely in the range where the release of intracellular Ca^{2+} has been observed in both osteoblasts and vascular endothelial cells.

The maximum fluid shear stress s_{max} (30) that the osteocytic process experiences is also a function of the loading frequency ω. This can be seen by noting that s_{max} (30) depends on $W(Y)$ and $W(Y)$, given by (31), depends upon the parameter β, where β is proportional to the square root of the loading frequency ω, $\beta=(1+i)\sqrt{\omega d^2/2c}$. This frequency dependence is important in examining the variation in s_{max} over the physiological frequency range 1–20 Hz associated with mechanical loading due to locomotion and posture. For a prescribed axial load, s_{max} is proportional to $|W|$ which has been plotted as a function of frequency for two representative values of M, 1 and 10, at $Y=0$ and ±1 (Fig. 12). Although $|W|$ is a complicated function of frequency, one observes that for frequencies less than about 25 Hz, the maximum fluid shear stress at all three values of Y varies nearly linearly with frequency for both $M=1$ and 10. This nearly linear dependence on ω can also be shown to hold for all other values of Y within the bone specimen provided ω is less than about 25 Hz. The new theory thus predicts that the fluid shear stress on the membrane is proportional to the product of σ and ω at physiological frequencies that include both low (locomotion) and high (postural) frequency mechanical loading.

DISCUSSION

We first provide an overview of our hypothesis for the mechanosensory transduction mechanism by which communicating osteocytes sense the very small *in vivo* strains in the calcified matrix components of bone. We propose that the osteocytes, although not responsive to substantial fluid pressures, can be stimulated by relatively small fluid shear stresses acting on the membranes of their osteocytic processes. We believe that these stresses lead to the release of intracellular Ca^{2+} that regulates the opening and closing of membrane ion channels in the communicating junctions linking the osteocytic processes at their apical ends. In this manner, the gap junctions modulate the intracellular potential and current that passes through the network of interconnected osteocytes and surface osteoblasts. Strong evidence in support of this view has recently been reported by Xia and Ferrier (1992). These investigators demonstrated using osteoblast cultures that mechanically induced intracellular currents are excited by the presence of intracellular Ca^{2+} and can easily propagate distances of the order of the thickness of a trabecula. It was further demonstrated that this Ca^{2+} elicited response can propagate through long tethered connections of

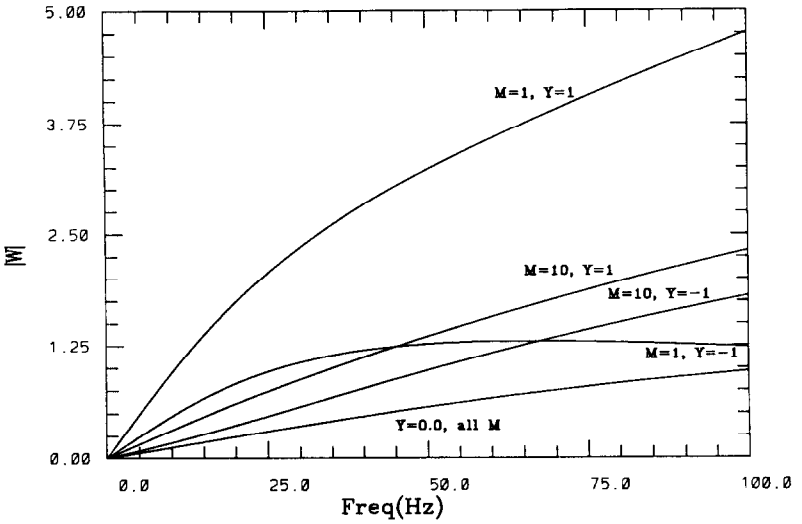

Fig. 12. A plot of the function $|W|$ on the membrane surface of the osteocytic processes, as a function of the frequency of the applied loading for a bending to axial load ratios $M=1$ and $M=10$, at different locations Y within the trabecular element for *in vivo* conditions, $P=0$ at $Y=\pm 1$. The results are for the model of a trabecula, in this model the trabecular thickness is $2d=200$ μm and the other canalicular parameters are chosen such that $\tau_r=0.0724$ s.

the type seen in osteocytes. These direct measurements of the propagation of intracellular potential changes due to Ca^{2+} support earlier studies by Jeansonne *et al.* (1979) of osteoblasts on the surface of rat pup calvaria which showed that current injected into a target cell could be measured several hundred μm from its source. While numerous other shear stress induced chemical responses have been observed in cell monolayers subject to fluid shear stress, to our knowledge, Ca^{2+} is the primary chemical agent that causes the configurational change in gap junction proteins that regulates intracellular potential. This regulation would be an important input into the recent model of Harrigan and Hamilton (1993) in which they propose that the intracellular current and potential are the electrical signals for the cellular detection of mechanical strain.

In our model, Biot's porous media theory has been used to relate the combined axial and bending loads applied to a whole bone to the flow past the osteocytic processes in their canaliculi. The fluid annuli that surround the osteocytic processes are assumed to be filled with aggregated PGs whose GAG is ordered by albumin. This assumption concerning the hypothesized arrangement of the PGs is based on analogy with many other cell membranes in a physiological fluid environment where ruthenium red staining has revealed a surface glycocalyx which in the presence of albumin appears to be ordered [see Michel (1988)]. The presence of a matrix of this type is essential if the model is to predict the measured pore pressure relaxation times and the observed fluid shear stresses for intracellular Ca^{2+} release. Furthermore, we shall show that there is only a narrow range of Δ, comparable to the size of the albumin molecule, where these predictions are possible. We now discuss each of the results in greater detail.

We begin with a discussion of the pore fluid pressure distributions in Fig. 8(d)–(f). The no-leakage ($\eta=0$) solution (29), has been thought (Salzstein *et al.*, 1987; Scott and Korostoff, 1990) to describe the capillary surface tension conditions associated with the measurement of the streaming potential in the four point bending apparatus. One can show that the second term in equation (29) is equivalent to equation (24) in Salzstein *et al.* (1987), and that the first term of equation (29) is due to the axial load, which is not considered in their analysis. Intuitively, one might expect the solution (29) to approach the solution given in Salzstein *et al.* (1987) when $M=10$, since the bending component of the applied load is large compared to the axial load. Rather surprisingly, the two solutions are similar only when $T\gg 1$ [Fig. 8(f)]. For $T\ll 1$ [Fig. 8(d)] the solutions for P show a nearly uniform pressure distribution across the specimen and a magnitude which is a hundred-fold larger than the curves in Fig. 8(a), where the solution for the $P=0$ wet surface boundary condition for $T=0.01$ is shown. The asymptotic analysis for $T\ll 1$ in the Appendix reveals that at very low frequencies, the solution in Salzstein *et al.* for the pore pressure will be in error if even a small axial loading component is present, if $MT<1$. The solution (A3) for $\eta=0$ and $T\ll 1$, shows that the leading term in the solution for P is due to the small axial load and is of $O(1/T)$ whereas the bending term in which M appears is of $O(1)$. The physical explanation for this behavior is that for $T\ll 1$, although a large bending moment may be applied, there is adequate time for this nonuniformity in pressure to be relieved. The integrated average load for bending is zero. In contrast, the pore pressure due to the axial component of the load cannot be relieved if there is no fluid flux at the lateral boundaries at $Y=\pm 1$. However, if the free flow boundary condition, $P=0$ ($\eta\to\infty$) at

$Y=\pm 1$, is used, the pore pressure due to the axial load can be relieved and the solution is very close to the quasisteady solution of equation (23) in which the time derivative term is omitted.

In the other limit, asymptotic analysis for $T \gg 1$ reveals, for both the free flow and no-leakage boundary conditions [Fig. 8(c) and (f)], that the unsteady solution of equation (23) with the $\partial^2 P/\partial Y^2$ term missing is valid everywhere except near the boundaries. Singular perturbation theory shows that the highest-order derivative term $\partial^2 P/\partial Y^2$ becomes important in narrow regions, in the vicinity of $Y=\pm 1$, whose thickness is of order $T^{-1/2}$. This boundary layer like correction occurs for either the $P=0$ or the $\partial P/\partial Y=0$ surface conditions. The solution for $T=1$ [Fig. 8(b) and (c)] show the transition between these two very different limiting behaviors.

The dependence of the pore fluid pressure relaxation time τ_r on the canalicular geometry ratio q and the dimensionless length ratio α is illustrated (Fig. 7) by the plot of equation (25). Recall that α is a ratio of the width of the fluid annulus $(b-a)$ to the thickness $\sqrt{k_p}$ of the fiber induced boundary layer. The data of Salzstein and Pollack (1987) and of Scott and Korostoff (1990) indicate that pore fluid pressure relaxation time τ_r is approximately 1.5 s. As noted previously, if we take q to be 2.8, and assume $\tau_r = 51$ s, one finds that these values of τ_r and q are compatible when $\alpha \cong 51$ (Fig. 7). This value of α has also been used in our companion study, Cowin *et al.* (1993), in which an electrokinetic theory is developed for the streaming potential in the canalicular annulus. The solution for the streaming potential, when $\alpha=51$, provides very good agreement with the measured phase and magnitude of the stress-generated potential over a frequency range that covers three orders of magnitude. Before examining the structure of the fiber matrix that corresponds to the predicted value of α, we shall first analyze the critical role that the fiber matrix plays in the solution and the importance of this large value of α.

In our previous and more primitive model, Weinbaum *et al.* (1991), we did not consider the presence of a PG matrix in the fluid annulus. This absence of the matrix led to major contradictions with experimental results that the present model is able to rectify. In the limit in which no matrix is present, the boundary layer associated with the fibers dominates the flow and α approaches zero. The velocity profile in this limit is a distorted parabola as shown by the inner profile in Fig. 3. The first contradiction is the predicted value of q (Fig. 7) for the pore pressure relaxation time $\tau_r = 1.5$ s determined by curve fitting the experimental data of Scott and Korostoff (1990) on frequency vs phase at the SGPs. The matrix free model, $\alpha=0$, predicts that $q=1.15$ if $\tau_r=1.5$ s, whereas a value of q between 2 and 3 is observed experimentally. The predicted width of the fluid annulus, approximately 2.0 nm, is only about one-fifth of that which has been observed. If we require instead that $q=2.5$ and $\alpha=0$, one finds that the pore relaxation time is less than 0.01 s (Fig. 7). This pore relaxation time is two orders of magnitude smaller than the experimental measurements of the pore relaxation time reported by Salzstein and Pollack (1987) and Scott and Korostoff (1990).

Consider next our solution for $\alpha=51$. When $\alpha \gg 1$, the matrix not only greatly increases the fluid resistance but significantly alters the velocity profiles near the boundaries and, hence, the shear stress at the membrane surface $r=a$ of the osteocytic process. One observes (Fig. 6) that predicted value of the ratio s/s_∞ for $\alpha=51$ when $q=2.5$ is only 0.03. The shear stress at the membrane surface is thus only 3% of the shear stress that would be experienced with the same loading if the fiber matrix were not present. As we shall show shortly, the maximum predicted shear stress during the loading cycle for physiological strains is of the order 10 dyn cm^{-2} when the matrix is present, $M=1$ and $\alpha=51$. This shear stress would increase to over 300 dyn cm^{-2} if $M=1$, $q=2.8$ and there were no matrix. This is a second contradiction, since fluid shearing stresses of this magnitude are not physiologically realistic. These large shearing stresses are known to detach endothelial cells from basement membrane [see Fry (1968)].

A major contribution of this paper is that it demonstrates that if a PG matrix with appropriate fiber spacing is contained in the lacunar–canalicular porosity, this porosity can serve as the pore system for fluid pressure relaxation. This conclusion differs from the conclusion of Salzstein *et al.* (1987) and of Salzstein and Pollack (1987) that the pore pressure relaxation occurs in 20–60 nm pores between the crystallites of the mineral hydroxyapatite and that these same pores are the pathway for their measured streaming potential in their four-point bending apparatus experiments. Their conclusion stems from a model identical to ours except that they did not have a fiber matrix in the lacunar–canalicular porosity and, therefore, concluded from their measured pore relaxation times that the pore pressure relaxation occurs in smaller dimensioned 20–60 nm pores between the crystallites of the mineral hydroxyapatite. In our companion study, Cowin *et al.* (1993), we show that the lacunar–canalicular porosity can also serve as the pathway for the streaming potential. This theory shows that the same matrix structure (i.e. value of α) required to predict the measured pore pressure relaxation time in the experiments of Salzstein and Pollack (1987) and Scott and Korostoff (1990) provides a best fit for the measured phase and magnitude of the SGP in these experimental studies. The location of the pores for the streaming potential are important in interpreting the results of an interesting model recently proposed by Harrigan and Hamilton (1993) for predicting the transmembrane potential difference between the intracellular and extracellular fluid of the osteocytes. Since the fluid exterior to the membrane of the osteocytic process is the canalicular fluid, their cable theory for bone cell signaling implicitly assumes that

the SGPs occur in the lacunar–canalicular porosity at the surface of the osteocytes.

Do the pores in the crystalline hydroxyapatite contribute to the bone fluid movement and the SGP in mature bone? We have assumed in our model that there is negligible fluid movement in the porosity between the crystallites of the mineral hydroxyapatite because this water is both bound by interaction with the ionic crystal and because the mature bone at the walls of the lacunar–canalicular system is relatively impermeable to bone fluid. Neuman and Neuman (1958) argue that the bone water in the porosity between the crystallites of the mineral hydroxyapatite is largely bound water. These authors note that there is a 10 nm thick hydration layer of bound water retained at centrifugations of 10,000 **g** around each hydroxyapatite crystal. Labeled tracer studies provide strong evidence in support of the hypothesis that the boundaries of the lacunar–canalicular system are impermeable. Studies with microperoxidase (2 nm diameter) and horseradish peroxidase (6 nm diameter), Doty and Schofield (1972), Tanaka and Sakano (1985) and Dillaman *et al.* (1991), all indicate that these tracers label the boundaries of the lacunar–canalicular system, the boundary plasmalemma of the osteocytes and matrix components in the canalicular fluid space, but do not appear to penetrate the mineralized matrix in mature rat bone. A different behavior is observed in bone that has not yet crystallized. Thus, in new born chick a larger tracer, ferritin (11 nm dia.), is rapidly convected from the Haversian system through the collagen tissue matrix before this matrix has mineralized, but rather surprisingly the ferritin tracer does not appear in the lacunae [see Dillaman (1983)]. This last observation will be discussed shortly in connection with our predictions for the fiber spacing Δ.

The results for k/k_∞ (Fig. 5) provide the critical insight into the role that the PG matrix plays in regulating the hydraulic conductivity of the bone tissue and explains why previous investigators have discounted the lacunar–canalicular porosity in earlier models for the pore pressure relaxation time (Johnson et al., 1982; Salzstein *et al.*, 1987). One observes that for our theoretically predicted value of $\alpha = 51$, corresponding to a pore pressure relaxation time of 1.5 s, the Darcy permeability k is two orders of magnitude smaller than k_∞, the permeability of the annulus without the matrix considered in Weinbaum *et al.* (1991). This predicted value of α can be directly related to our hypothesized structure for the PG matrix shown in Fig. 4 . As noted in the results (Fig. 10) the predicted value of Δ, for $q = 2.8$ and $\alpha = 51$, is very close to 7 nm, the effective diameter of albumin. This value of Δ has been systematically measured using different size molecular tracers in numerous studies of other tissues that function as capillary filters for plasma proteins. These studies provide convincing evidence that albumin orders the GAG components of the matrix and determines their spacing (Curry, 1986; Michel, 1988). No equivalent systematic experimental studies have been conducted for the fiber matrix in the lacunar–canalicular porosity, but the studies with HRP and ferritin cited earlier provide valuable bounds. HRP (6 nm dia.) is able to quickly penetrate the lacunar–canalicular space and thus the fiber spacing must be larger than this molecule, as it is in capillary endothelium. Ferritin (11 nm dia.), on the other hand, does not appear to fill the fluid space surrounding the osteocytes in their lacunae, even in new born chick bone where the bone tissue has not yet been mineralized (Dillaman, pers. commun.). This suggests that either the walls of the lacunar–canalicular system are impermeable to this molecule, which would seen unlikely if the matrix is not mineralized, or that the surface glycocalyx surrounding the osteocyte is an effective sieve for this molecule. These observations suggest that Δ lies somewhere between 6 and 11 nm.

The fluid shear stresses predicted (Fig. 11) are remarkably close to the range of shear stresses, 10 to 20 dyn cm^{-2}, where an adaptive remodeling of the vasculature has been observed so as to maintain nearly constant endothelial fluid shear stress throughout the entire arterial side of the circulation [see Kamiya *et al.* (1984)]. To understand the origin of this response, several investigators have conducted tissue culture experiments in which confluent monolayers of bovine aortic endothelial cells grown in culture have been exposed to laminar shear flow. Since the original study by Ando *et al.* (1988), which first demonstrated that intracellular Ca^{2+} is released in response to the fluid shear, many investigators have attempted to elucidate the details of this response. The cell culture studies of Dull and Davies (1991) suggest that endothelial cells do not respond to the absolute magnitude of the shear stress but to changes in the stress level of as little as 0.25 dyn cm^{-2}. The experiments of Shen *et al.* (1990) show a threshold stress of 0.4 dyn cm^{-2} and a saturation stress for the release of intracellular Ca^{2+} of 4 dyn cm^{-2}. The study by Geiger *et al.* (1992) showed that the response could not be eliminated by the removal of extracellular Ca^{2+}. Finally, in preliminary results just reported on rat calvarial osteoblasts, Williams *et al.* (1992), have shown a closely related behavior with a threshold for the excitation of the full Ca^{2+} response of 6 dyn cm^{-2}. This increase in intracellular Ca^{2+} was independent of the level of fluid shear stress in the range 6–30 dyn cm^{-2}. These results, while still speculative, are of special significance for our overall hypothesis since osteoblasts are progenitors of osteocytes and have the capability of propagating Ca^{2+} induced currents and electrical signals over distances comparable to the dimensions of a trabecula or an osteon (Jeansonne *et al.*, 1979; Xia and Ferrier, 1992).

A recent finding with important implications as to the nature of the mechanosensory signal that causes bone tissue to maintain its mass is the observation by McLeod and Rubin (1993) that high-frequency mus-

cular contractions to maintain posture, which are of the order of 250 μstrain and thus much smaller than the 1000–3000 μstrain encountered during locomotion (Lanyon, 1984; Rubin and Lanyon, 1984, 1987), can be instrumental in maintaining and increasing bone mass. Measurements of the mechanical strain in the long bones of three species (horse, dog and wild turkey) have shown periodic oscillations of typically 15–25 Hz. When peak low amplitude postural strains of 250 μstrain were introduced into the isolated turkey ulna at a frequency of only 1 Hz, there was a significant net loss of bone after only four weeks, while the same amplitude loading at 15 Hz caused a substantial increase in bone mass. This result is consistent with the observation of Rubin and Lanyon that the threshold for maintaining bone mass at 1 Hz due to locomotion is 1000 μstrain. This intriguing and unexpected dependence on frequency, rather than just magnitude of mechanical loading, is consistent with the predictions of our model (Fig. 12). The results in this figure show that the fluid shear stress on the membrane is nearly proportional to the product of σ and ω for all frequencies below 25 Hz. This linear response is consistent with the measurements on turkey ulna in McLeod and Rubin where the loss or increase in bone mass at each frequency was shown to be proportional to σ. According to our model (Fig. 12) a postural strain of 250 μstrain at 15 Hz will produce a fluid shear stress that is 3.75 times that of a 1000 μstrain loading due to locomotion at 1 Hz and thus far exceed the threshold for excitation. This calculation suggests that low amplitude postural strains due to muscular contractions could be more effective than high-amplitude low-frequency strains due to locomotion in maintaining bone mass. The theory, therefore, suggests that the bone cells are just as likely to be excited by low-amplitude postural strains due to muscular contractions as high-amplitude low-frequency strains due to locomotion. Such behavior might explain why astronauts in a microgravity environment, where the need to maintain posture is absent, lose bone mass despite rigorous exercise.

The theoretical predictions in this paper have important implications for the possible nature of the excitation process that controls stress related resorption and deposition of bone tissue. Our model calculations suggest that the same type of surface glycocalyx that is present on vascular endothelium is also attached to the membranes of the osteocytic processes and fills the canalicular fluid space surrounding the process. The theoretical predictions for the open gap Δ between the GAG components of the surface glycocalyx has a predicted mean value that is approximately 7 nm. This dimension is remarkably close to the size of the albumin molecule, which a large body of evidence now suggests orders the PG matrix at the surface of the cells. Our theoretical predictions for the fluid shear stress on the membranes of the osteocytic processes correspond closely to the experimentally measured range of stresses, where Ca^{2+} has been observed to be released from intracellular stores in shear stress activated endothelial cells and osteoblasts. This release of Ca^{2+}, we believe, is important in the regulation of intracellular currents and transmembrane potential differences and is consistent with the recent experiments, Xia and Ferrier (1992), on Ca^{2+} induced electrical signaling between osteoblasts. Finally, the new model is consistent with intriguing observations of McLeod and Rubin (1993) that low-amplitude high-frequency postural strains can maintain or increase bone mass. It would be unlikely for a coincidence of these separate relationships to occur and thus it is the combined coincidence of all these observations that provides the strongest argument for the validity of the model that we have proposed.

Acknowledgements—The contribution of SCC was supported by NSF Grant No. BSC-9103236 and by grant number 662319 from the PSC-CUNY Research Award Program of the City University of New York. The authors thank Dr. Richard A. Salzstein of the Hercules Inc. Research Center, Professors Letty Moss-Salentijn and Melvin L. Moss of Columbia University, Professor Richard M. Dillaman of the University of North Carolina at Wilmington and Dr. Stephen Doty of the Hospital for Special Surgery for helpful discussions and references. We also thank K. J. McLeod and J. L. Williams for pre-publication copies of their papers.

REFERENCES

Ando, J., Komatsuda, T. and Kamiya, A. (1988) Cytoplasmic calcium response to fluid shear stress in cultured vascular endothelial cells. *In Vitro*, **24**, 871–877.

Atkinson, P. J. and Hallsworth, A. S. (1982) The spatial structure of bone. In *Progress in Anatomy* (Edited by Harrison, R. J. and Navaratnam, V). pp. 179–199. Cambridge University Press, Cambridge.

Atkinson, P. J. and Hallsworth, A. S. (1983) The changing pore structure of aging human mandibular bone. *Gerodontology* **2**, pp. 57–66.

Baud, C. A. (1976) Histophysiology of the osteocyte; an introduction to the morphology of periosteocytic lacunae. In *Proc. 1st Workshop on Bone Morphometry* (Edited by Jaworski, Z. F. G.), pp. 267–272. University of Ottawa Press, Ottawa.

Biot, M. A. (1941) General theory of three-dimensional consolidation. *J. appl. Phys.* **12**, 155–164.

Biot, M. A. and Willis, D. G. (1957) The elastic coefficients of the theory of consolidation. *J. appl. Mech.* **24**, 594–601.

Brinkman, H. C. (1947) A calculation of the viscous force exerted by a flowing fluid on a dense swarm of particles. *Physica* **13**, 447–457.

Cane, V., Marotti, G., Volpi, G., Zaffe, D., Palozzini, S., Remaggi, F. and Muglia, M. A. (1982) Size and density of osteocytic lacunae in different regions of long bones. *Calcif. Tissue Int.* **34**, 558–563.

Cowin, S. C. (1989) *Bone Mechanics*. CRC Press, Boca Raton, FL.

Cowin, S. C., Weinbaum, S. and Zeng, Yu (1993) A case for the bone canaliculi as the anatomical site of strain generated potentials. *J. Biomechanics* (submitted)

Curry, F. E. (1986) Determinants of capillary permeability: a review of mechanisms based on single capillary studies in the frog. *Circ. Res.* **59**, 367–380.

Curry, F. E. and Michel, C. C. (1980) A fiber matrix model of capillary permeability. *Microvasc. Res.* **20**, 96–99.

Dillaman, R. M. (1984) Movement of ferritin in the 2 day-old chick femur. *Anat. Record* **209,** 445–453.
Dillaman, R. M., Roer, R. D. and Gay, D. M. (1991) Fluid movement in bone: theoretical and empirical. *J. Biomechanics* **24** Supplement, 163–177.
Doty, S. B. and Schofield, B. H. (1972) Metabolic and structural changes within osteocytes of rat bone. In *Calcium, Parathyroid Hormone and the Calcitonins* (Edited by Talmage, B. V. and Munson, P. L.), pp. 353–365. Excerpta Medica, Amsterdam.
Dull, R. O. and Davies, P. F. (1991) Flow modulation of agonist (ATP)-response (Ca^{2+}) coupling in vascular endothelial cells. *Am. J. Physiol.* **261,** H149–H154.
Fry, D. L. (1968) Acute vascular endothelial changes associated with increased blood velocity gradients. *Cir. Res.* **22,** 165–182.
Geiger, R. V., Berk, B. C., Alexander, R. W. and Nerem, R. M. (1992) Flow-induced calcium transients in single endothelial cells: spatial and temporal analysis. *Am. J. Physiol.* **262** (*Cell Physiol.* 31), C1411–C1417.
Harrigan, T. P., and Hamilton, J. J. (1993) Bone strain sensation via transmembrane potential changes in surface osteoblasts: loading rate and microstructural implications. *J. Biomechanics* **26,** 183–200.
Heinegård, D. and Oldberg, A. (1989) Structure and biology of cartilage and bone matrix noncollagenous macromolecules. *FASEB J.* **3,** 2042–2051.
Jande, S. S. (1971) Fine structural study of osteocytes and their surrounding bone matrix with respect to their age in young chicks. *J. Ultrastructure Res.* **37,** 279–300.
Jande, S. S. and Bélanger, L. F. (1971) Electron microscopy of osteocytes and the pericellular matrix in rat trabecular bone. *Calcif. Tissue Res.* **6,** 280–289.
Jeansonne, B. G., Feagin, F. F., McMinn, R. W., Shoemaker, R. L. and Rehm, W. S. (1979) Cell-to-cell communication of osteoblasts. *J. dent. Res.* **58,** 1415–1423.
Johnson, M. W. (1984) Behavior of fluid in stressed bone and cellular simulation. *Calcif. Tissue Int.* **36,** S72–S76.
Johnson, M. W., Chakkalakal, D. A., Harper, R. A., Katz, J. L. and Rouhana, S. W. (1982) Fluid flow in bone. *J. Biomechanics* **11,** 881–885.
Kamiya, A., Bukhari, R. and Togawa, T. (1984) Adaptive regulation of wall shear stress optimizing vascular tree function. *Bull. Math. Biol.* **46,** 127–173.
Knese, K.-H. (1979) Stuzgewebe und Skelettsystem. *Handbuch mikroskop. Anat. d. Mencschen 2: Die Gewebe, Part 5.* Springer, Berlin.
Krstic, R. V. (1978) *Die Gewebe des Menschen und der Saugetiere.* Springer, Berlin.
Kufahl, R. H. and Saha, S. (1990) A theoretical model for stress-generated fluid flow in the canaliculi-lacunae network in bone tissue. *J. Biomechanics* **23,** 171–180.
Lanyon, L. E. (1984) Functional strain as a determinant for bone remodeling. *Calcif. Tissue Int.* **36,** S56–S61.
Luft, J. H. (1966) Fine structure of capillary and endocapillary layer as revealed by ruthenium red. *Federation Proceedings* **25,** 1773–1783.
Marotti, G. (1980) Three dimensional study of osteocytic lacunae, *Metab. Bone. Dis. Rel. Res.* **2,** S223–229.
McLeod, K. J., and Rubin, C. T. (1993) Strain oscillations in functionally loaded bone: a species independent determinant of skeletal morphology. *J. Biomechanics* (submitted).
Michel, C. C. (1988) Capillary permeability and how it may change. *J. Physiol.* **404,** 1–29.
Morris, M. A., Lopez-Curato, J. A., Hughes, S. P. F., An, K. N., Bassingthwaighte, J. B. and Kelly, P. J., (1982) Fluid spaces in canine bone and marrow. *Microvasc. Res.* **23,** 188–200.
Neuman, W. F. and Neuman, M. W. (1958) *The Chemical Dynamics of Bone.* University of Chicago Press, Chicago.
Nowinski, J. L. and Davis, C F. (1970) A model of the human skull as a poroelastic spherical shell subjected to a quasi-static load. *Math. Biosci.* **8,** 397–416.
Nowinski, J. L. and Davis, C. F. (1972) The flexure and torsion of bones viewed as poroelastic bodies. *Int. J. Engng Sci.* **10,** 1063–1079.
Owen, M. and Triffitt, J. T. (1976) Extravascular albumin in bone tissue. *J. Physiol.* **257,** 293–307.
Palumbo, C. (1986) A three dimensional ultrastructural study of osteoid-osteocytes in the tibia of chick embryos. *Cell Tissue Res.* **246,** 125–131.
Pickarski, K. and Munro, M. (1977) Transport mechanism operating between blood supply and osteocytes in long bones. *Nature* **269** (5623), 80–82.
Pollack, S. R., Petrov, N., Salzstein, R., Brankov, G. and Blagoeva, R. (1984) An anatomical model for streaming potentials in osteons. *J. Biomechanics* **17,** 627–636.
Poole, A. R. (1986) Proteoglycans in health and disease: structures and functions. *Biochem. J.* **236,** 1–14.
Rice, J. R. and Cleary, M. P. (1976) Some basic stress diffusion solutions for fluid-saturated elastic porous media with compressible constituents. *Rev. Geophys. Space Phys.* **14,** 227–241.
Rubin, C. T. and Lanyon, L. E. (1984) Regulation of bone formation by applied dynamic loads. *J. Bone Jt Surg.* **66A,** 397–410.
Rubin, C. T. and Lanyon, L. E. (1987) Osteoregulatory nature of mechanical stimuli: function as a determinant for adaptive bone remodeling. *J. ortho. Res.* **5,** 300–310.
Salzstein, R. A., Pollack, S. R., Mak, A. F. T. and Petrov, N. (1987) Electromechanical potentials in cortical bone-I. A continuum approach. *J. Biomechanics* **20,** 261–270.
Salzstein, R. A. and Pollack, S. R. (1987) Electromechanical potentials in cortical bone-II. Experimental analysis. *J. Biomechanics* **20,** 271–280.
Sangani, A. S. and Acrivos, A. (1982) Slow flow past periodic arrays of cylinders with application to heat transfer. *Int. J. Multiphase Flow* **8,** 193–205.
Scott, G. C. and Korostoff, E. (1990) Oscillatory and step response to electromechanical phenomena in human and bovine bone. *J. Biomechanics* **23,** 127–143.
Shen, J., Luscinskas, F. W., Connolly, A., Dewey, C. F. J. and Gimbrone, M. A. J. (1990) Fluid shear stress modulates intracellular ionized calcium in vascular endothelial monolayers. In *Proc. First World Congress of Biomechanics* (Edited by Woo, S. L. Y., Wayne, J. S. and MacKenna, D. A.), Vol. 2, p. 196.
Tanaka, T. and Sakano, A. (1985) Differences in permeability of microperoxidase and horseradish peroxidase into alveolar bone of developing rats. *J. dent. Res.* **64,** 870–876.
Tsay, R.-Y. and Weinbaum, S. (1991) Viscous flow in a channel with periodic cross-bridging fibers: exact solutions and Brinkman approximation. *J. Fluid Mech.* **226,** 125–148.
Weinbaum, S., Cowin, S. C. and Zeng, Yu (1991) A model for the fluid shear stress excitation of membrane ion channels in osteocytic processes due to bone strain. In *Proc. Advances in Bioengineering 1991* (Edited by R. Vanderby, Jr) pp. 317–320. Am. Soc. Mech. Engrs, New York.
Williams, J. L. (1992) Ultrasonic wave propagation in cancellous and cortical bone: prediction of some experimental results by Biot's theory. *J. Acoust. Soc. Am.* **91,** 1106–1112.
Williams, J. L., Iannotti, J. P., Ham, A., Bleuit, J. and Chen, J. H. (1992) The influence of laminar flow on intracellular calcium in isolated bone cells. *J. orthop. Res* (submitted).
Xia, S.-L. and Ferrier, J. (1992) Propagation of a calcium pulse between osteoblastic cells. *Biochem. biophys. Res. Commun.* **186,** 1212–1219.

APPENDIX

When $T \ll 1$, the governing equation (23) for the pore pressure can be simplified using perturbation theory in which we let T be a small parameter. We introduce a perturbation solution of the form $P = P_0/T + P_1$ for the pressure and introduce a stretched time variable $\hat{\tau} = T\tau$ which is of

order unity when τ is of order $1/T$. When these new variables are introduced into equation (23) and terms of the same order in T are equated, we find that to $O(1)$

$$\frac{\partial^2 P_0}{\partial Y^2}=0, \tag{A1}$$

while to $O(T)$ we have

$$\frac{\partial P_0}{\partial \tilde{\tau}}-\frac{\partial^2 P_1}{\partial Y^2}=(1+MY)\cos\tilde{\tau}. \tag{A2}$$

Equation (A1) satisfies the boundary condition $\partial P_0/\partial Y=0$ at $Y=\pm 1$, and equation (A2) satisfies the boundary condition $\partial P_1/\partial Y=0$ at $Y=\pm 1$. The solution to equation (A1) for P_0 is an arbitrary function of time and independent of the Y coordinate. This arbitrary function can be determined from the $O(T)$ boundary value problem for P_1. After some analysis, one can show that the solution to equation (23), to the first two orders in the small parameter T, is

$$P=\frac{1}{T}\sin\tilde{\tau}+\frac{1}{2}MY\left(1-\frac{Y^2}{3}\right)\cos\tilde{\tau}+O(T). \tag{A3}$$

One notes that in equation (A3) the coefficient of the leading term is of $O(1/T)$ and independent of M, whereas the term in which M first appears is of $O(1)$. Thus, remarkably, to the lowest order the solution does not include bending and the highest-order forcing term in the solution is due to the axial load. The effect of bending is a cubic polynomial in Y. This term becomes comparable to the axial term only if MT is of order unity.